



UPPSALA
UNIVERSITET

*Digital Comprehensive Summaries of Uppsala Dissertations
from the Faculty of Science and Technology 1890*

Solid-state nanopores

fabrication and applications

SHUANGSHUANG ZENG



ACTA
UNIVERSITATIS
UPSALIENSIS
UPPSALA
2020

ISSN 1651-6214
ISBN 978-91-513-0838-8
urn:nbn:se:uu:diva-399726

Dissertation presented at Uppsala University to be publicly examined in Polhemsalen, Ångströmlaboratoriet, Lägerhyddsvägen 1, Uppsala, Friday, 21 February 2020 at 09:15 for the degree of Doctor of Philosophy. The examination will be conducted in English. Faculty examiner: Professor Amit Meller (Technion Israel Institute of Technology).

Abstract

Zeng, S. 2020. Solid-state nanopores. fabrication and applications. *Digital Comprehensive Summaries of Uppsala Dissertations from the Faculty of Science and Technology* 1890. 82 pp. Uppsala: Acta Universitatis Upsaliensis. ISBN 978-91-513-0838-8.

Nanopores are of great interest in study of DNA sequencing, protein profiling and power generation. Among them, solid-state nanopores show obvious advantages over their biological counterparts in terms of high chemical stability and reusability as well as compatibility with the existing CMOS fabrication techniques. Nanopore sensing is most frequently based on measuring ionic current through a nanopore while applying a voltage across it. When an analyte passes through the pore, the ionic current temporarily changes, providing information of the analyte such as its size, shape and surface charge. Although many magnificent reports on using solid-state nanopores have appeared in the literature, several challenges still remain for their wider applications, which include improvement of fabrication reproducibility for mass production of ultra-small nanopores and minimization of measurement instability as well as control of translocation speed and reduction of background noise. This thesis work explores different techniques to achieve robust and high throughput fabrication of sub-10 nm nanopores for different applications.

The thesis starts with presenting various fabrication techniques explored during my PhD studies. Focused ion beam method was firstly employed to drill nanopores in free-standing SiN_x membranes. Sub-10 nm nanopores could be obtained with a focused helium ion beam. But the fabrication throughput was limited with this technique. A new fabrication process combining electron beam lithography (EBL) with reactive ion etching/ion beam etching, which is compatible with the existing CMOS fabrication technology, was developed to realize a high throughput, mass production of nanopores in free-standing SiN_x membranes. However, the smallest size that could be controllably achieved with this process was around 40 nm, which is still far from sub-10 nm in size required for, e.g., DNA sequencing. Finally, by using anisotropic etching of single-crystal silicon in KOH solution, sub-5 nm truncated pyramidal nanopores were mass produced with good process controllability in a silicon-on-insulator (SOI) substrate. In addition, nanopore arrays were also successfully fabricated using a modified EBL based fabrication process.

Then, several sensing application examples using either single nanopores or nanopore arrays were investigated. Translocation of nanoparticles, DNA and proteins were demonstrated using the fabricated single nanopores or nanopore arrays in a single freestanding membrane. Moreover, the kinetics and mechanism of the lipid bilayer formation in nanopore array, aiming to prevent non-specific adsorption, were studied using ionic current measurements. In addition, individual addressability of a solid-state nanopore array on separated freestanding membranes was realized by integrating microfluidics and a customized multiplexer.

Keywords: solid-state nanopore, truncated-pyramidal nanopore, nanopore array, pore size reduction, individual addressability, microfluidics, translocation.

Shuangshuang Zeng, Department of Electrical Engineering, Solid-State Electronics, Box 534, Uppsala University, SE-751 21 Uppsala, Sweden.

© Shuangshuang Zeng 2020

ISSN 1651-6214

ISBN 978-91-513-0838-8

urn:nbn:se:uu:diva-399726 (<http://urn.kb.se/resolve?urn=urn:nbn:se:uu:diva-399726>)

To my family, to my friends

List of Papers

This thesis is based on the following papers, which are referred to in the text by their Roman numerals.

- I Wen C.*, **Zeng S.***, Arstila K., Sajavaara T., Zhu Y., Zhang Z., & Zhang S. L. (2017). Generalized noise study of solid-state nanopores at low frequencies. *ACS Sensors*, 2(2), 300-307.
- II Wen C., **Zeng S.**, Zhang Z., & Zhang S. L. (2018). Group behavior of nanoparticles translocating multiple nanopores. *Analytical Chemistry*, 90(22), 13483-13490.
- III **Zeng S.***, Wen C.*, Zhang S. L., Solomon P., & Zhang, Z. (2019). Rectification of protein translocation in truncated-pyramidal nanopores. *Nature Nanotechnology*. 14(11), 1056–1062.
- IV **Zeng S.**, Wen C., Li S., Chen X., Chen S., Zhang S. L., & Zhang Z. (2019). Controlled size reduction and its underlying mechanism to form solid-state nanopores via electron beam induced carbon deposition. *Nanotechnology*, 30(45), 455303.
- V **Zeng S.***, Li S.*, Utterström. U., Wen C., Selegård R., Zhang S. L., Aili D., & Zhang Z. (2019). Mechanism and kinetics study of lipid bilayer formation in solid-state nanopores. Under review in *Langmuir*.
- VI **Zeng S.***, Wen C.*, Zhang S. L., & Zhang Z. (2019). A nanopore array of individual addressability enabled by integrating microfluidics and a multiplexer. *IEEE Sensors Journal*, DOI: 10.1109/JSEN.2019.2947713

* The authors contributed equally to the work.

Reprints were made with permission from the respective publishers.

Author's contributions

- I. Performed the nanopore device fabrication and partially contributed to building up the measurement setup, took part in discussion including handling referee comments and wrote part of the manuscript including revising the manuscript in accordance to referee comments.
- II. Performed the nanopore device fabrication and characterization, took part in discussion including handling referee comments and wrote part of the manuscript including revising the manuscript in accordance to referee comments.
- III. Performed the nanopore device fabrication and characterization, took part in discussion including handling referee comments and wrote part of the manuscript including revising the manuscript in accordance to referee comments.
- IV. Planned and performed most of the experimental work apart from the COMSOL simulation and nanoparticle translocation, took part in discussion including handling referee comments and wrote the manuscript including revising the manuscript in accordance to referee comments,
- V. Planned and performed most of the experimental work apart from the fluorescence microscopy observation, took part in discussion including handling referee comments and wrote the manuscript including revising the manuscript in accordance to referee comments.
- VI. Planned and performed most of the experimental work apart from the multiplexer design and manufacture, took part in discussion including handling referee comments and wrote the manuscript including revising the manuscript in accordance to referee comments.

Publications not included in this thesis

- I. Wen, C., **Zeng, S.**, Li, S., Zhang, Z., & Zhang, S. L. (2019). On rectification of ionic current in nanopores. *Analytical chemistry*, 91(22), 14597-14604.
- II. Li, S., **Zeng, S.**, Zhang, Z., Hjort, K., & Zhang, S. L. (2019, June). Nanoparticle Localization on Solid-State Nanopores Via Electrophoretic Force. In *2019 20th International Conference on Solid-State Sensors, Actuators and Microsystems & Eurosensors XXXIII (TRANSDUCERS & EUROSENSORS XXXIII)* (pp. 2372-2375). IEEE.
- III. Wen, C., Li, S., **Zeng, S.**, Zhang, Z., & Zhang, S. L. (2019). Auto-genic analyte translocation in nanopores. *Nano Energy*, 60, 503-509.
- IV. Hu, Q., Chen, X., Norstrom, H., **Zeng, S.**, Liu, Y., Gustavsson, F., Zhang, S. L., Chen, S., & Zhang, Z. (2018, September). Current gain and low-frequency noise of symmetric lateral bipolar junction transistors on SOI. In *2018 48th European Solid-State Device Research Conference (ESSDERC)* (pp. 258-261). IEEE.
- V. Li, S., **Zeng, S.**, Chen, L., Zhang, Z., Hjort, K., & Zhang, S. L. (2018). Nanoarrays on Passivated Aluminum Surface for Site-Specific Immobilization of Biomolecules. *ACS Applied Bio Materials*, 1(1), 125-135.
- VI. Zhao, J., **Zeng, S.**, Wu, B., Zhang, S. L., & Zhang, Z. B. (2018). Re-organized graphene nanoplatelet thin films achieved by a two-step hydraulic method. *Diamond and Related Materials*, 84, 141-145.
- VII. Wen, C., **Zeng, S.**, Zhang, Z., Hjort, K., Scheicher, R., & Zhang, S. L. (2016). On nanopore DNA sequencing by signal and noise analysis of ionic current. *Nanotechnology*, 27(21), 215502.

Contents

1. Introduction.....	15
1.1 Biosensors	16
1.2 Nanopore sensors	17
1.3 Challenges in solid-state nanopore sensing.....	18
1.4 Outline of this thesis.....	18
2. Basic theory of solid-state nanopore sensing.....	20
2.1 Working principle of solid-state nanopore sensors	20
2.2 Noise spectrum.....	21
2.3 Nanopore conductance and size determination	22
2.4 Electrical double layer.....	24
2.5 Electrophoresis	25
2.6 Electroosmosis	27
3. Fabrication and characterization of solid-state nanopores	28
3.1 Nanopore fabrication by FIB milling	30
3.2 Nanopore fabrication by the combination of EBL and RIE	31
3.3 Nanopore fabrication by combination of EBL and ion beam etching (IBE).....	33
3.4 Nanopore fabrication by wet chemical etching.....	34
3.5 Nanopore size reduction by electron beam induced carbon deposition (EBICD).....	40
3.6 Nanopore size reduction by lipid bilayer coating.....	45
4. Sensing applications with single nanopores.....	47
4.1 Nanoparticle translocation through a SiN _x nanopore with its size reduced by EBICD	47
4.2 DNA translocation through TPPs.....	49
4.3 Protein translocation through TPPs.....	50
4.4 Enzymatic reaction monitoring with TPPs.....	53
5. Sensing applications of nanopore array	56
5.1 Single free-standing membrane with multiple nanopores	56
5.1.1 SiN _x nanopore array for nanoparticle translocation.....	56
5.1.2 TPP array for lipid bilayer formation	59
5.2 Multiple free-standing membranes with single nanopore on each.....	65

6. Summary and outlook	68
Sammanfattning på Svenska	70
Acknowledgement	73
References.....	75

Abbreviations

2D	Two-dimensional
AeL	Aerolysin
ALD	Atomic layer deposition
BOX	Buried oxide
BSE	Backscattered electron
CDB	Controlled dielectric breakdown
ClyA	Cytolysin A
DNA	Deoxyribonucleic Acid
DRIE	Deep reactive ion etching
EBICD	Electron beam induced carbon deposition
EBL	Electron beam lithography
EDL	Electrical double layer
EDP	Ethylenediamine pyrocatechol
EDX	Energy dispersive X-ray spectroscopy
EOF	Electroosmotic flow
FIB	Focused ion beam
FTE	Frequency of translocation event
GO _x	Glucose oxidase
HGP	Human Genome Project
HIM	Helium ion microscope
IPA	2-propanol
I-V	Current-voltage
KCl	Potassium chloride
KOH	Potassium hydroxide
LPCVD	Low pressure vapor deposition
MspA	Mycobacterium smegmatis porin A
OmpG	Outer membrane protein G
PDMS	Polydimethylsiloxane
PBS	Phosphate buffered saline
PE	Primary electron
pI	Point of isoelectric
PM	Precision Medicine
POPC	1-palmitoyl-2-oleoyl-glycero-3-phosphocholine
PSD	Power spectral density
PZC	Potential of zero charge
RIE	Reactive ion etching

RNA	Ribonucleic acid
SE	Secondary electron
SEM	Scanning electron microscope
SiN _x	Low stress silicon nitride
SiO ₂	Silicon dioxide
SOI	Silicon on insulator
STD	Standard deviation
TEM	Transmission electron microscope
TMAH	Tetramethylammonium hydroxide
TPP	Truncated pyramidal nanopore
α -HL	α -hemolysin
a	side length of the bottom base of a TPP
A	normalized noise power defined as $A=\alpha/N_c$
C_{chip}	capacitance of the dielectric materials composing the membrane and support structure
C_{total}	total capacitance
d	diameter of the pore
D	dielectric loss
e_n	equivalent voltage noise at the op-amp input
E	electric field
f	frequency
G	conductance of the nanopore
I	ionic current
I_{ave}	average current through a multiple pore system
I_e	ionic current at equilibrium
I_o	open pore current
I_t	ionic current at time t
k	rate constant
L	opening size in the top of a TPP
L_{eff}	effective transport length
k	Boltzmann constant
M	mol/L
N	number of pores in a multi-pore system
N_c	number of charge carriers
N_{SRP}	number of size reduced pores
P_{50s}	events (<i>i.e.</i> current drops) within the first 50 s over the whole 500 s timespan
r	radius of the charged species
R	resistance of the nanopore
S	minimum cross section area in the nanopore
R_H	hydrodynamic radius
$S(f)$	PSD of total current noise
S_{IC}	PSD of capacitance noise
S_{ID}	PSD of dielectric noise
S_{IF}	PSD of flicker noise

S_{IT}	PSD of thermal noise
t	thickness of the nanopore
T	absolute temperature in degrees Kelvin
v_{ep}	electrophoretic velocity
v_{EOF}	EOF velocity
α	Hooge parameter,
β	exponent in flicker noise
ΔI	amplitude of blockage caused by the translocation
ε	permittivity of the fluid
ζ	surface potential of the charged surface
η	dynamic (shear) viscosity of the fluid
θ	wedge angle of the nanopore
μ_{ep}	electrophoretic mobility
ρ	resistivity of the electrolyte
τ_b	mean dwell time of blockage stage
τ_o	mean dwell time of open pore state

1. Introduction

Although the Egyptian Imhotep described the diagnosis and treatment of 200 diseases in 2600 BC and the Greek Hippocrates established the scientific study of medicine in 460 BC [1], they lacked a deep understanding of disease biology. After the Industrial Revolution in the 18th century, people made tremendous scientific discoveries and inventions together with the rapid economic and industrial growth. Since then significant progress has been made in understanding the function of microorganisms and identifying the origins of illness. Vaccines have been developed to prevent diseases including measles, polio, influenza and cervical cancer. In 1990, the Human Genome Project (HGP) was formally launched. The goal was to sequence and understand all the genes of human beings. HGP was declared complete in April 2003 at a cost of around US\$3 billion [2]. After more than a decade, the sequencing cost has been decreasing dramatically with the advancement of modern technology, as shown in Figure 1.1. Many genomes can now be sequenced in a day for around \$1,000 each [3]. Until now, most medical treatments have been designed in a ‘one-size-fits-all’ approach. However, the treatments can only be successful for some patients rather than for all of them. Genetic insights can help doctors take their patients’ uniqueness into account when prescribing treatments. This is actually transforming the way of diseases treatment. For example, molecular tests are routinely performed to get the genetic information of the patients with breast or lung cancers, which provides an opportunity to achieve precise personalized patient care [4] thus facilitating precision medicine (PM). The individualized nature of PM requires personalized diagnostics and the technologies needed to perform such diagnostics have been rapidly evolving. Biosensors, which combine electronics, photonics, advanced materials, microfluidics and chemistry, offer great promises for rapid, portable and easy-to-use diagnosis [5].

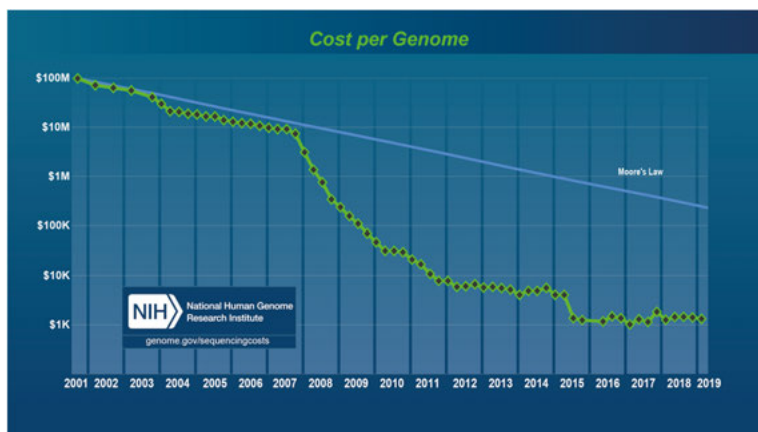


Figure 1.1. Sequencing cost per genome [3].

1.1 Biosensors

Biosensors generally consist of three parts: a recognition component that can interact with the analyte and produce a signal, a transducer that can transform one signal into another one in a physicochemical way, and a readout device that can amplify and process the transformed signal. Biosensors can be classified based on the type of biorecognition element, or on the mode of transduction. With the former classification, biosensors can be mainly divided into enzymatic, aptamer-based, nucleic acid-based, antibody-based and whole-cell based biosensors. With the latter classification, biosensors can be mainly divided into electrochemical, optical, thermal, piezoelectric and electrical biosensors [6]– [9]. A comparison of different types of biosensors is given in the the table below. In this thesis, a kind of electrical biosensors named nanopore sensors, which are based on the ionic current measurement, is presented.

Table 1.1. Comparison of different types of biosensors classified by the transduction mode.

Transduction mode	Types	Pros	Cons
Electrochemical	Potentiometric		
	Amperometric	Label- free, simple, easy	Possible drift of the signal, lack of
	Impedimetric	automation, low cost, fast	specificity
	Conductometric		
Optical	Fluorescence		
	Chemiluminescence	Real-time measurement,	Costly equipment, not portable,
	Surface Plasmon Resonance	high sample throughput	labeling required
Thermal	Micro Calorimetry	Label- free, rapid	High cost, possible fouling

Piezoelectric	Surface Acoustic Wave	High sensitivity, fast, label-free, simple, chemically inert	Lack of specificity and sensitive to external disturbances
	Quartz Crystal Microbalance		
Electrical	Field Effect Transistor	Label- free, simple	Low specificity
	Nanopore		

1.2 Nanopore sensors

Nanopore sensors provide a newly emerging technique for the detection of biomolecules such as DNA, RNA and polypeptides. Nanopore based sensing is a simple and label-free single molecule recognition approach. It requires very low sample volumes without sample amplifications. Nanopores can be broadly classified into three categories: biological pores embedded in a lipid bilayer, solid-state pores fabricated in thin solid films and hybrid of biological and synthetic pores [10], [11].

In the 1990s, it was proposed that nucleic acid sequence could be determined with nanopore detection if single nucleotide resolution could be achieved [12]. In 1996, Kasianowicz and co-workers demonstrated that single stranded DNA was electrophoretically driven through a biological pore α -hemolysin (α -HL) and generated ionic current drops during the translocation [13]. This is the first report of using nanopore for nucleic acid sensing. Since this landmark demonstration of nucleic acid detection with α -HL, a wide variety of biological nanopores with various characteristics including OmpG [14], MspA [15], AeL [16] and ClyA [17] have been discovered and used for sensing applications [18], [19]. So far, Oxford Nanopore Technologies has released the commercialized nanopore based DNA/RNA sequencers: MinION, GridION and PromethION, enabling ultra-long reads, rapid, direct and real-time data analysis [20]. Although one of the main driving forces behind the nanopore sensing is its potential to sequence DNA rapidly and inexpensively, numerous efforts have also been attempted in many other fields such as detection of proteins [21], [22], small molecules [23], [24] as well as metal ions [25].

Stepping into the 21st century, solid-state nanopores are developed to complement the limitations of their biological counterparts including fixed pore size, mechanical and chemical instabilities. They can be fabricated in different materials such as silicon nitride [26], [27], silicon oxide [28], aluminum oxide [29], graphene [30], and molybdenum disulfide [31]. Various techniques including ion beam sculpting, focused electron beam drilling, controlled dielectric breakdown, combination of electron beam lithography (EBL) and reactive ion etching (RIE) and directed laser drilling have been reported for nanopore fabrication [32].

1.3 Challenges in solid-state nanopore sensing

For solid-state nanopores, although lots of fascinating work has been performed [33]– [35], several challenges remain for their wider applications. Firstly, achieving an optimal translocation speed is highly desired for nanopore sensing. It has been reported that the translocation speed of DNA through nanopores is >10 nt/ μ s for solid-state pores and >1 nt/ μ s in α -HL and MspA pores [36]. The mean protein translocation times are around 1 μ s [37]. Signal bandwidth exceeding 1 MHz will be required to have sufficient temporal resolution to perform the task, which is not available for most of the commercialized amplifiers [38]. Moreover, background noise will also increase as the bandwidth increases. Therefore, additional measures need to be taken to slow down the translocation of the analyte. With the introduction of enzymes, DNA translocation could be slowed down to 2.5–70 nt/sec [39], [40]. Secondly, reducing the noise in solid-state nanopores is crucial to achieve a high signal to noise ratio. Various efforts have been made to reduce the noise: passivating the nanopore with PDMS [41] or photoresist [42] to reduce the exposed area to the electrolyte solution; inserting a thick oxide layer underneath the nanopore membrane [38], [43]; using different substrates as a replacement of silicon [44], [45]. Thirdly, minimizing the sensing region is required to reach a high spatial resolution. Thickness of the pore membrane greatly influences the size of the sensing region. Two-dimensional (2D) materials such as graphene [46] and molybdenum disulfide [31] with their atomic thickness provide a good solution addressing this issue. Fourthly, addressing the instability issue of the measurements is key to achieving reliable and precise sensing results. Various sources can lead to the instability of the measurements. For example, the size of nanopore can grow slowly over time [47]. Non-specific adsorption of the analyte on the nanopore also causes the variation of the measurement [48]. It is noteworthy that pore to pore variations exist even though nanopores have the identical conductance and similar geometry [49]. Attentions need to be paid to have a well-controlled surface of the nanopores. Last but not least, mass production of solid-state nanopores with high size uniformity is also very important for potential commercialization.

1.4 Outline of this thesis

This thesis presents my efforts in the development of nanopore sensors. The main focus is to explore different techniques for fabricating sub-10 nm sizes nanopores with mass production potential. Underlying mechanisms of certain techniques are discussed. Several nanopore sensing applications are demonstrated. Following the general introduction in this chapter, the rest of the thesis is organized as follows:

Chapter 2 introduces the basic theory of nanopore sensing, including the sensing principle, noise sources, conductance model and basic physics of the driving forces of the analyte movement through a nanopore.

Chapter 3 summarizes the various techniques I have explored to fabricate nanopores on either silicon nitride or silicon membranes.

Chapter 4 presents several sensing applications with single nanopores fabricated by different techniques.

Chapter 5 describes the attempts of nanopore array fabrication and applications.

Chapter 6 will conclude this work and give a brief outlook of the future works.

2. Basic theory of solid-state nanopore sensing

To date, most of the nanopore sensing studies are based on resistive pulse sensing technique using electrical signals for molecule detection and identification. The precedent of resistive pulse sensing is the Coulter counter, which was developed in the 1950s for counting particles suspended in a fluid through a micrometer-sized hole [50]. Reducing the aperture size down to the nanoscale led to the birth of modern nanopore sensors. In this chapter, we will firstly illustrate the working principle of solid-state nanopore sensors based on resistive-pulse sensing. Then we will discuss the dominant sources of current noise in different frequency regimes, which greatly limits the sensitivity of nanopore sensors. We will also introduce the conductance model and equations to determine the nanopore size based on the measured conductance. Finally, we will brief the basic physics of electrical double layer, electrophoresis and electroosmosis, which are needed to understand the driving forces in nanopore sensing.

2.1 Working principle of solid-state nanopore sensors

A complete measurement setup is schematically illustrated in Figure 2.1. The nanopore chip is mounted on a custom-made flow cell and sealed using two O-rings on the two sides. Two reservoirs are then filled with electrolyte and separated by the chip. An Ag/AgCl electrode is immersed on each side of the membrane to apply a bias voltage across the nanopore. The resulting ionic current through the nanopore is measured using a dedicated low noise amplifier. The flow cell is embedded in a tight metallic enclosure (primary Faraday cage) to shield electromagnetic interference. A secondary Faraday cage is used to provide an additional electromagnetic shielding. The whole setup is positioned on an anti-vibration table to minimize the noise induced by mechanical vibrations. The analog signals from the current amplifier are digitized with a data acquisition card. When molecules to be detected pass through the pore, obstructions of the pore by the molecules result in decreases of the ionic current. The amplitude, duration, and frequency of these transient current changes can be used to determine the detected molecules' characteristics such as size, surface charge, geometry as well as their interactions with the pores.

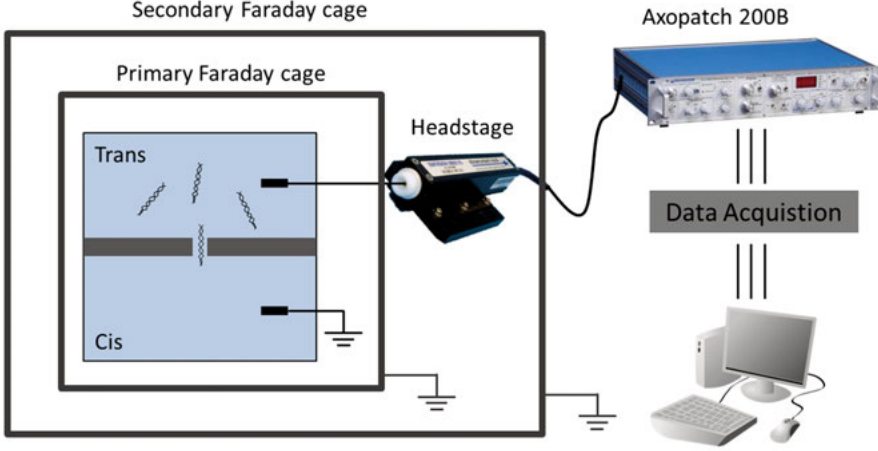


Figure 2.1. Schematic diagram of a complete nanopore measurement setup.

2.2 Noise spectrum

Both noise and bandwidth of ionic current recordings need to be taken special care of to obtain high a signal-to-noise ratio and sufficient temporal resolution using nanopore sensors. Different noise sources have distinct frequency dependences (see Figure 2.2) and the total current noise power spectral density (PSD) can therefore be broken down into components by fitting PSD to a polynomial form [51], [52]:

$$\begin{aligned}
 S(f) &= S_{IF} + S_{IT} + S_{ID} + S_{IC} \\
 &= \frac{AI^2}{f^\beta} + \frac{4kT}{R} + 8\pi kTDC_{chip}f + (2\pi fC_{total})^2 e_n^2 \quad (2.1)
 \end{aligned}$$

where f is the frequency, S_{IF} , S_{IT} , S_{ID} and S_{IC} represent the contributions from the flicker, thermal, dielectric, and capacitance noises, respectively; A is the normalized noise power defined as $A = \alpha/N_c$ in the Hooge model [53], [54], N_c denotes the number of charge carriers, and α the Hooge parameter, which quantifies the level of flicker noise, the exponent β is typically unity, but has been observed to vary [41], [52]; k is Boltzmann constant, T is absolute temperature in degrees Kelvin, R is the resistance of the nanopore; D is the dielectric loss, C_{chip} is the capacitance of the dielectric materials composing the membrane and support structure; C_{total} is the total capacitance, and e_n is the equivalent voltage noise at the op-amp input.

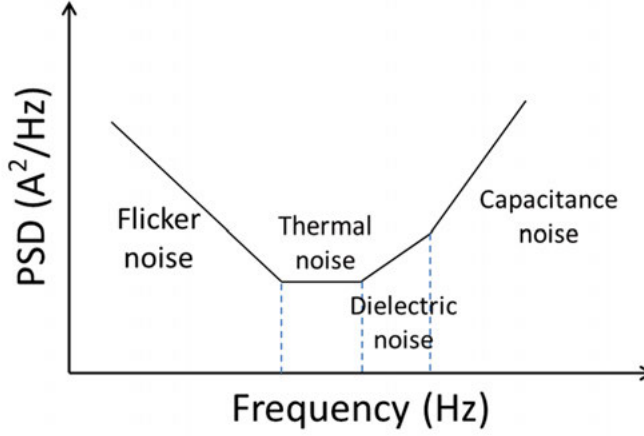


Figure 2.2. Dominant sources of current noise power spectral density, illustrated as a function of frequency.

2.3 Nanopore conductance and size determination

A solid-state nanopore can be considered to consist of three sensing regions: The interior of the nanopore itself and an access region on either side [55]. Therefore, the conductance of a cylindrical nanopore can be described as [56]:

$$G = \left(\frac{4\rho t}{\pi d^2} + \frac{\rho}{d} \right)^{-1} \quad (2.2)$$

where ρ is the resistivity of the electrolyte, t is the thickness of the membrane and d is the diameter of the pore. The first term in the parentheses describes the resistance in the interior volume of the pore and the second term represents the access resistance of the access region [57]. However, for nanopores with other shapes such as hour-glass, cone and truncated pyramid, the description of the conductance requires sophisticated mathematical calculation. Wen *et al* introduced a new conductance model based on the concept of effective transport length L_{eff} [58]. L_{eff} originates from the electric field (E) distribution in a nanopore and is defined to be the sum of the distances from the center of the nanopore, where the electric field intensity is at its maximum (E_{max}), to the two points along the nanopore axis in both upward and downward direction, where the electric field intensity falls to e^{-1} of its maximum. The conductance can be described as:

$$G = \frac{S}{\rho L_{eff}} \quad (2.3)$$

where S is the minimum cross section area in the nanopore.

For instance, the diameter of the nanopore can be calculated to be:

$$L_{eff} = t + 0.92d \quad (2.4)$$

$$d = \frac{1.84G\rho + \sqrt{3.39G^2\rho^2 + 4\pi tG\rho}}{\pi} \quad (2.5)$$

for cylindrical pores (Figure 2.3(a)), which can be used for determining nanopore diameter of our fabricated SiN_x nanopores.

For truncated pyramidal nanopores: When the upper part of concentrated electric field region ($E > E_{max}/e$) lies in the nanopores (Figure 2.3(b)),

$$L_{eff} = 0.525a(1 + \sqrt{\frac{1}{1 - \sin\theta}}) \quad (2.6)$$

$$a = 0.525 \left(1 + \frac{1}{\sqrt{1 - \sin\theta}} \right) G\rho \quad (2.7)$$

When the upper part of concentrated electric field region ($E > E_{max}/e$) extends outside of the nanopores (Figure 2.3(c)),

$$L_{eff} = 1.05a + t(1 - \sqrt{1 - \sin\theta}) \quad (2.8)$$

$$a = \frac{1.05G\rho + \sqrt{1.1025G^2\rho^2 + 4(1 - \sqrt{1 - \sin\theta})tG\rho}}{2} \quad (2.9)$$

where a is the side length of the bottom base of truncated pyramidal nanopores, θ is the wedge angle of the nanopore. These two equations can be used to determine the size (*i.e.* the bottom base) of our silicon based, truncated pyramidal nanopore, where $\theta = 54.7^\circ$.

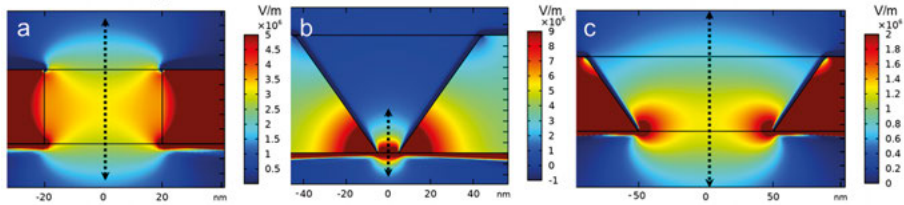


Figure 2.3. Simulation results of the electric field distribution in a nanopore with 150 mM KCL solution at -200 mV (a) A cylindrical nanopore with $d=40$ nm in 25 nm thick SiN_x, (b) A truncated pyramidal nanopore with $a=10$ nm in 55 nm thick Si, (c) A truncated pyramidal nanopore with $a=100$ nm in 55 nm thick Si. The dashed line with two arrows denotes the L_{eff} region in each figure.

2.4 Electrical double layer

When immersing a solid surface in an electrolyte solution, the surface becomes charged. The excess charge on the surface attracts the ions of opposite polarity (counterions) in the solution to reach local charge neutrality and result in an accumulation of ions with opposite polarity near it. Ions with same polarity as the surface charge (co-ions) are depleted in this region due to the effects of entropy and Coulomb repulsion [59]. The cumulative result is known in electrochemistry as the electrical double layer (EDL). According to the Gouy-Chapman-Stern model [60], the EDL consists of a layer of adsorbed ions, named the Stern layer, and a layer of mobile ions, called the diffuse layer. The slip plane is an imaginary plane separating ions that are immobile at the surface from those that are mobile in solution [61]. The ζ potential at this plane can be experimentally determined and be used to estimate the surface potential. The ζ potential is dependent on the pH and ionic strength of the solution [62]. At a specific pH value of the solution, the solid surface bears no net charge, known as the point of zero charge (PZC). PZC for silicon nitride and silicon oxide is 4.1 [63] and 2.8 [64], respectively. At the physiological pH of 7.4, silicon nitride is negatively charged. Figure 2.4 shows a schematic diagram of the charge distribution at the SiN_x /electrolyte interface at pH=7.4. Another important characteristic parameter of the EDL is the Debye length and it corresponds to the thickness of the EDL. The Debye length increases as the electrolyte concentration decreases. In 1 M KCl and 1 mM KCl solution, the Debye length is around 0.3 nm and 10 nm, respectively [61].

For a nanopore sensor, EDL is formed not only on the sidewalls of nanopore, but also surrounding the analytes to be detected including DNA, proteins and nanoparticles. Electrostatic forces are created as a result of surface charge and play an important role for long-range interactions between molecules and nanopore surfaces.

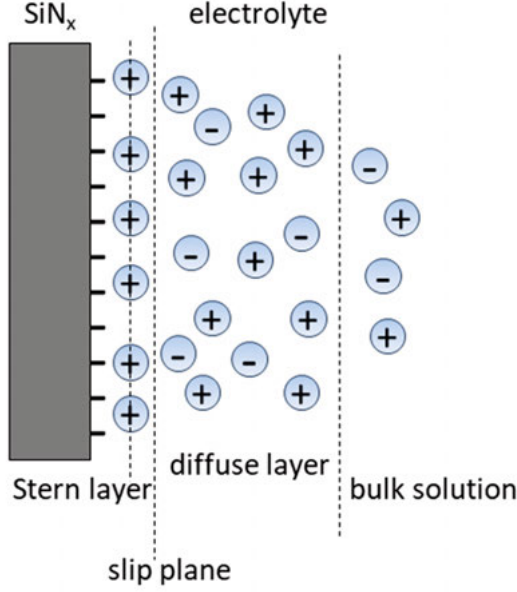


Figure 2.4. Schematic diagram of the EDL at the SiN_x /electrolyte interface at $\text{pH}=7.4$.

2.5 Electrophoresis

Electrophoresis is a common technique used to migrate and separate charged species (ions or particles) under an electric field. The electrophoretic mobility of a charged species, μ_{ep} , is defined as the proportionality factor between the electrophoretic velocity, v_{ep} , and the electric field, E [65]:

$$v_{ep} = \mu_{ep} E \quad (2.10)$$

Under an electric field, charged species suspended in the electrolyte solution undergo forces resulting from Coulombic interaction, viscous drag, polarization, inertia, and random thermal motion [66]. Depending on the thickness of the EDL compared to the size of charged species, the electrophoretic mobility can be divided into two categories. For ions and some small proteins, which can be identified as point charge, the EDL thickness is comparable to their size. The electrophoretic mobility can be expressed as [67]:

$$\mu_{ep} = \frac{q}{6\pi\eta r} \quad (2.11)$$

where q is the charge carried by the species, η is the dynamic (shear) viscosity of the fluid and r is the radius of the charged species. If the EDL thickness is

much smaller than the size of the charged species, the electrophoretic mobility is given by [61]:

$$\mu_{ep} = \frac{\varepsilon \zeta}{\eta} \quad (2.12)$$

where ε is the permittivity of the fluid, ζ is the ζ potential of the charged surface, and η is the dynamic (shear) viscosity of the fluid.

DNA is widely adopted in nanopore sensing field with the initial goal of using nanopores for DNA sequencing. Phosphate groups making up each nucleotide along the backbone of DNA are negatively charged in an aqueous solution of physiological pH of 7.4. Therefore, DNA molecules are highly negatively charged and electrophoresis is the dominant force for DNA translocation through nanopores [13]. However, these charged groups are partially screened by concentrated counter-ions in the vicinity of DNA [68], the effective charge per base pair is found experimentally to be around 0.06 elementary charge [69].

2.6 Electroosmosis

If an electric field is applied tangential to a solid-state surface with fixed charge to drive the motion of the ions in the liquid, the mobile ions with the opposite polarity in the EDL will move and draw the liquid adjacent to the surface due to the viscous interactions. This is known as electroosmosis. The resulting flow is termed electroosmotic flow (EOF). If the Debye length is much smaller than the pore size, the velocity of the EOF in the nanopore can be approximately as [61]:

$$v_{EOF} = -\frac{\varepsilon\zeta E}{\eta} \quad (2.13)$$

where ε is the permittivity of the fluid, ζ is the ζ potential of the charged surface, E is the electric field, and η is the dynamic (shear) viscosity of the fluid. For moderately or neutrally charged nanoparticles such as certain proteins, EOF instead of electrophoresis plays a dominant role on their translocation through the nanopores [70]–[72].

3. Fabrication and characterization of solid-state nanopores

Currently, there are many techniques to fabricate solid-state nanopores. Although the first controllable fabrication of solid-state nanopores was achieved by ion beam sculpting in 2001 [26], the most popular method nowadays is to use focused high energy electron beam in a transmission microscope (TEM) to directly drill the nanopores in a commercially available SiN_x TEM window [27]. Focused ion beam (FIB) has also been employed to drill nanopores in various membranes [73], [74]. Nonetheless, both methods suffer from big limitations on their fabrication throughput and cost efficiency. Controlled dielectric breakdown (CDB) provides a simple and cost-effective method by applying a high electric field across the dielectric membrane to perforate the membrane [75]. But the position of the nanopore fabricated using this method is difficult to control owing to the stochastic nature of the breakdown process [76]. Wet chemical etching [77], ion track etching [78], and combination of electron beam lithography (EBL) and reactive ion etching (RIE) [28], [79] have also been explored to pursue mass production of nanopores. Apart from the aforementioned direct nanopore fabrication techniques, there are also many other techniques employed to reduce the size of pre-fabricated nanopores such as atomic layer deposition [80], electron beam evaporation [81] and oxidation [28], [82]. The table below gives a comparison among different fabrication techniques. During my PhD studies, I started to use FIB to drill nanopores in SiN_x free-standing membranes (**Paper I**). TEM was not used due to the complicated operation and limited sample size. Then I switched to use EBL and RIE to fabricate nanopores aiming at high throughput and mass production. Both silicon nitride (**Paper II**) and silicon (**Paper III**) membranes have been used to fabricate nanopores. Additional methods including electron beam induced carbon deposition (**Paper IV**) and lipid bilayer coating (**Paper V**) to further reduce the size of pre-fabricated nanopores have also been explored.

Table 3.2. Comparison among different techniques for solid-state nanopore fabrication

Fabrication technique	Advantages	Disadvantages	Membrane material	Pore geometry	Reference
Ion beam sculpting	shrinking or enlarging pore by fine-tuning the ion beam exposure time and temperature; feedback control.	low throughput; sophisticated	Si ₃ N ₄ , SiO ₂	bowl shape	[26], [83]
TEM	direct visual feedback; nanometer precision; good repeatability	low throughput; sample size limitation; laborious	Si ₃ N ₄ , Al ₂ O ₃ , HfO ₂ , metal, MoS ₂	hour-glass shape	[27], [31], [84]–[86]
FIB	universal; efficient	difficult to reach sub-10 nm; re-deposition of sputtered material	Si ₃ N ₄ , SiC, Si, graphene, h-BN	hour-glass shape	[73], [87], [88]
CDB	fast; simple; sub-nm precision; low cost	difficult to control the position of the pore	SiN _x , MoS ₂	unknown	[75], [89]
Wet chemical etching	high throughput; simple	difficult to reach sub-10 nm	single crystal Si of (100) direction	truncated pyramidal shape	[77], [90]
Ion track etching	pore shape adjustable; ease of surface modification; sub-10 nm achievable	thick membrane; heavy ion accelerators required	polyethylene terephthalate, polycarbonate, polyimide	conical or cylindrical shape	[78], [91]–[93]
EBL and RIE	high throughput; compatibility with CMOS process;	difficult to reach sub-20 nm	SiN _x , SiO ₂ , Si	cylindrical shape	[79], [94], [95]
Glass nanocapillary	ease of fabrication	low throughput; difficult to reach sub-10 nm	borosilicate, quartz	conical shape	[96]–[98]

3.1 Nanopore fabrication by FIB milling

The fabrication of solid-state nanopores generally consists of two major steps: free-standing membrane formation and nanopore creation. The fabrication with FIB milling started with a 300 μm thick double side polished (100) orientation silicon wafer. The wafer was then oxidized to grow a 50 nm thick SiO_2 layer and a 20 nm thick low-stress SiN_x was deposited by means of low-pressure vapor deposition (LPCVD). Subsequently, a 425 $\mu\text{m} \times 425 \mu\text{m}$ square window was opened on the rear side of the wafer by photolithography and RIE. The bulk silicon substrate was then wet etched in KOH (30 wt%, 80 $^\circ\text{C}$, 5 h), followed by oxide stripping in buffered HF (40 s). These process steps made the 20 nm thick SiN_x on the front side a free-standing membrane. Finally, the nanopores were drilled with a focused gallium (Ga) ion beam on a FIB system (FIB, Strata DB235, FEI Company) with an operation voltage of 30 kV, or with a focused helium ion beam (He FIB) on a Helium Ion Microscope (HIM, Zeiss Orion). Nanopores with different sizes were fabricated by changing the exposure time and/or beam current. Fabrication process flow is schematically illustrated in Figure 3.1.

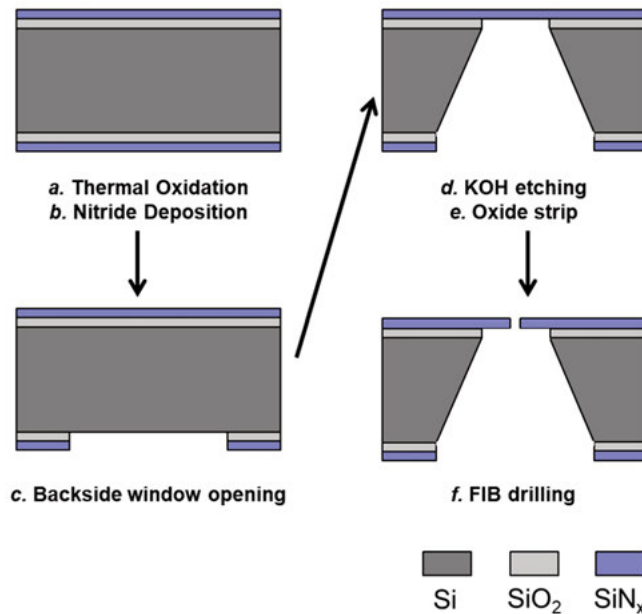


Figure 3. 1. Schematic illustration of the fabrication process for SiN_x nanopores by FIB drilling.

Figure 3.2(a) shows a FIB image of a 200 nm SiN_x drilled by the Ga FIB. As can be clearly seen, the pore has a crater shape, which was caused by the re-deposition of sputtered membrane material during Ga FIB drilling. However, the smallest size of such FIB drilled pores I have achieved is around 40 nm

and it is difficult to further reduce due to the limitations of the fine focus of the ion beam in a low beam current, beam diameter, beam shape, re-deposition as well as relatively thick membranes [73]. Compared with the Ga FIB, He FIB has some clear advantages such as reduced momentum transfer from the ion beam to the target material stemming from the lower mass of He relative to Ga [74], atomically small tip [75], and higher resolution. In collaboration with a research group in Finland where He FIB is accessible, a few attempts were made to drill sub-10 nm nanopores in SiN_x . Figure 3.2(b) shows a TEM image of a 7.2 nm SiN_x pore drilled by HIM.

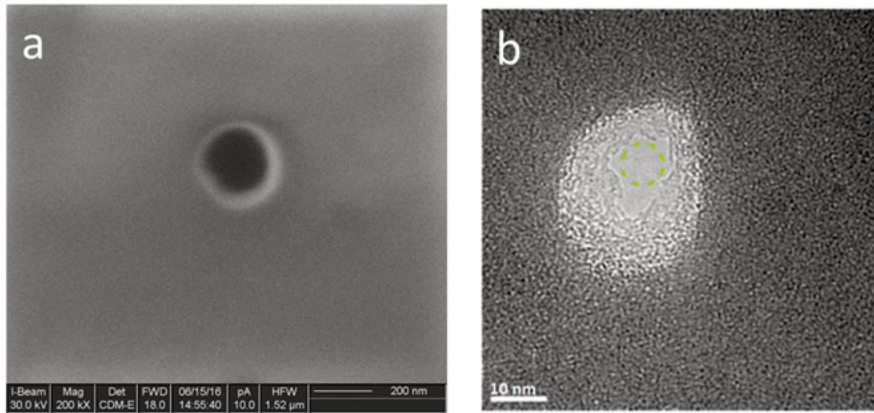


Figure 3. 2. FIB image of a 200 nm SiN_x pore drilled by FIB (a) and TEM image of a 7.2 nm SiN_x pore drilled by HIM.

3.2 Nanopore fabrication by the combination of EBL and RIE

The fabrication throughput of FIB drilling is greatly limited. Aiming at high throughput and mass production of solid-state nanopores, a new CMOS technology compatible fabrication process by combining EBL with RIE was explored. EBL and RIE were employed to fabricate nanopores with tunable and controllable sizes in SiN_x membranes. Figure 3.3 shows the detailed fabrication process flow. In brief, starting from a 300 μm (100) double side polished wafer with 50 nm SiO_2 and 20 nm SiN_x on both sides, nanoholes were patterned in the e-beam resisit on the front side with EBL and then transferred into the underlying SiN_x layer by RIE. Next, a 150 μm window was opened on the rear side with alignment to the nanopores on the front side using photolithography and RIE. It is noteworthy that a protective coating layer can be optionally put on the front side during the following KOH etching to minimize the enlargement of predefined SiN_x pore since SiN_x is attacked by KOH at a rate of around 1 nm/hour. Finally, deep reactive ion etching (DRIE) and KOH

etching was carried out to etch away the bulk silicon and buffered HF was used to strip the SiO_2 on the front side. A combination of DRIE and KOH etching was used here, instead of the previous KOH etching to shorten the wet etching time (1.5 h vs 5 h) and meanwhile maintain relatively small free-standing membrane area. If only DRIE was used, etching rate was limited at a high aspect ratio and it was difficult to obtain a small free-standing membrane.

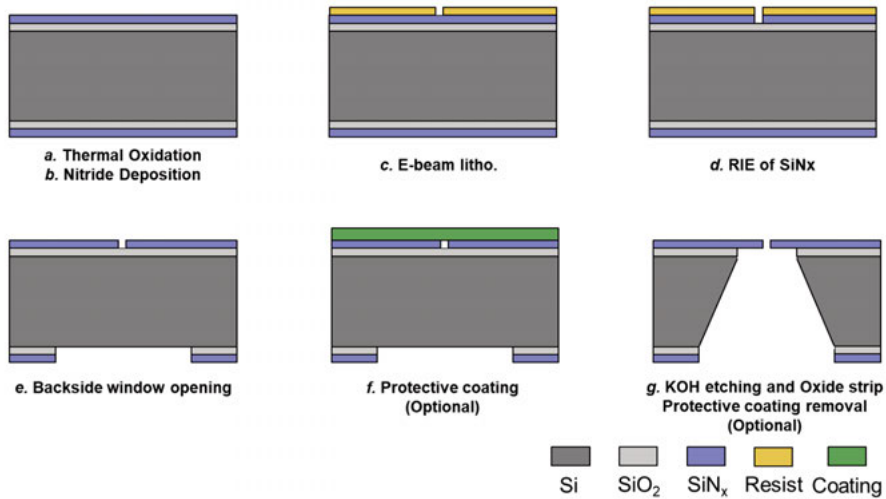


Figure 3. 3. Schematic illustration of the fabrication process for SiN_x nanopores by combination of EBL and RIE.

Figure 3.4 presents a set of SEM images of fabricated SiN_x nanopores ranging from 20 nm to 80 nm. To obtain a high contrast of the SEM image, the bulk silicon is not removed here. However, nanopores with the diameter of 20 nm or 30 nm are not highly reproducible owing to the resolution of the E-beam resist and enlargement during RIE. The nanopores in free-standing SiN_x with diameters >40 nm can be fabricated with very good reproducibility.

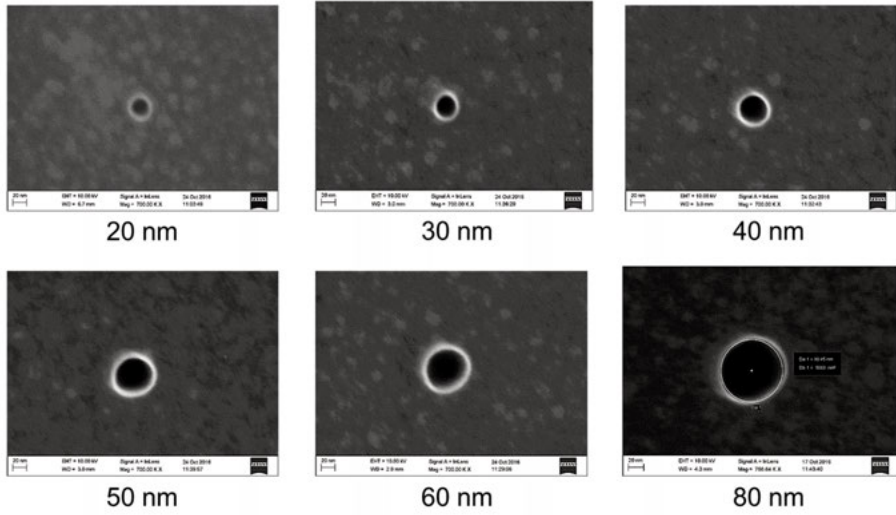


Figure 3. 4. SEM images of fabricated nanopores ranging from 20 nm to 80 nm.

3.3 Nanopore fabrication by combination of EBL and ion beam etching (IBE)

RIE is essentially a combination of highly selective chemical reaction and highly directional ion bombardment. High etching rate, high selectivity and high directionality can be obtained with RIE. However, it is often difficult to etch a specific material when there is no chemical etchant available. IBE, a physical etching process with almost no selectivity, is a good alternative for such tasks. IBE uses a stream of highly energetic Ar^+ ions to bombard and erode the sample surface (similar to the conventional sputtering). An attempt was made to etch EBL patterned nanopores in a SiN_x layer and the results are shown in Figure 3.5. IBE opens up the possibilities to fabricate nanopores in other materials such as metal layers (e.g. Au) or dielectric layers (e.g. Al_2O_3), which are difficult to realize with chemical etching methods. However, the available ion beam etcher in our cleanroom has a uniform etching area around 2 cm in diameter, which is much smaller than a 4 inch wafer. Therefore, IBE was not widely adopted for our nanopore fabrication.

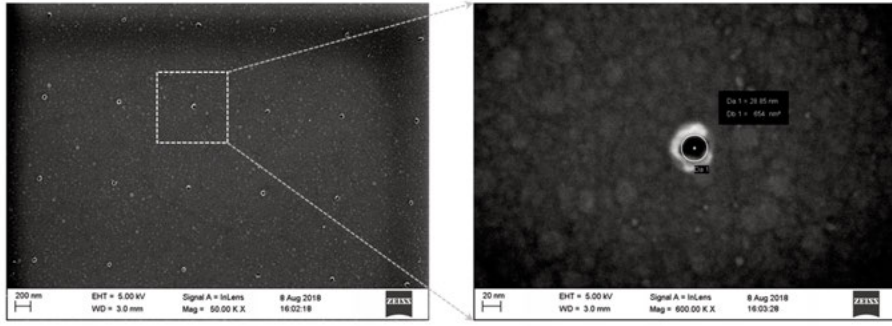
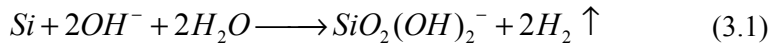


Figure 3. 5. SEM images of SiN_x nanopore array with diameter around 30 nm fabricated by ion beam milling.

3.4 Nanopore fabrication by wet chemical etching

Process parameters of pore exposure with EBL as well as etching directionality and selectivity of RIE can be further optimized to reproducibly obtain nanopores with diameters below 20 nm [81], [95]. But it will require a lot of tedious work and even so, sub-10 nm nanopores will be difficult to reach owing to the resolution of e-beam resist. Fortunately, nanopore size can be further reduced from the size defined by EBL by the anisotropic etching of single-crystal Si in Si wet etching solution. The wet etching solution can be KOH or other aqueous alkaline solutions such as tetramethylammonium hydroxide (TMAH) and ethylenediamine pyrocatechol water (EDP or EPW). The wet etching rate is highly dependent on the orientation of the crystallographic plane of the Si substrate [100], [101]. In all kinds of alkaline solutions, (111) plane is the slowest etching planes, while (110), (100) and other high index planes are the fast etching planes. Therefore, in the case of (100) silicon wafers, stable etched profiles are shaped by the slowest etch rate planes (*i.e.* (111)) [102] and V-grooves are formed by the exposed (111) plane oriented at an angle of 54.7° to the wafer surface during the etching process. As depicted in Figure 3.6(a), the opening size a in the bottom is determined as a linear relation: $a = L - \sqrt{2}t$, where L is the opening size in the top and t is the membrane thickness. By varying L , a will change correspondingly.

The overall reaction for the KOH etching process can be summarized by the following equation [100]:



The driving force for the overall reaction is given by the larger Si-O binding energy of 193 kcal/mol as compared to a Si-Si binding energy of only 78 kcal/mol [103]. No significant influence of the cations can be found and thus cations do not appear in the reaction equations. The etch rate is strongly dependent on the KOH concentration and temperature, and the maximal etch rate

occurs at a KOH concentration of 10-15 wt% [100]. Moreover, the etch rate is significantly affected by the impurities of the substrate and additives in the etchant. Etch rate decreases dramatically for silicon substrate heavily doped with boron (above $2 \times 10^{19} \text{ cm}^{-3}$) [101]. Additions of 2-propanol (IPA) or surfactant in the etchant also ensure a significant reduction in the etch rate [104].

KOH etching of Si is highly selective to other materials and various materials including SiO_2 , SiN_x and Cr can be used as hard mask layer. In our work, SiN_x is chosen owing to its extremely slow etching rate in KOH (1 nm/h in 30 wt% KOH at 80 °C). On a (100) Si wafer, significant undercut takes place at the edges that are not aligned along $\langle 110 \rangle$ direction owing to the appearance of (111) planes, as shown in Figure 3.6(b). Therefore, the final dimensions of the etched pattern can be much larger than desired. For EBL patterned nanoholes in the mask layer, the circular shape of the pattern doesn't require to be aligned with the $\langle 110 \rangle$ directions to minimize the undercut (Figure 3.6(c)). In this way, the final dimensions of the nanopores formed in silicon can be easily controlled.

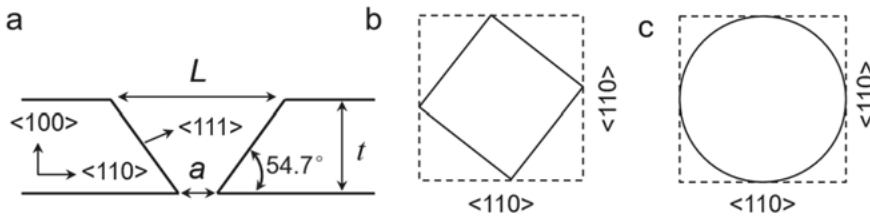


Figure 3. 6. Anisotropic etching of silicon. (a). A schematic drawing of anisotropic etching of (100) silicon from a side view. (b) Etched profile (dashed line) using a square mask not aligned with $\langle 110 \rangle$ direction on a (100) Si wafer from a top view. (c) Etched profile (dashed line) using a circular mask on a (100) Si wafer from a top view.

By making use of the KOH etching of silicon, truncated pyramidal nanopores (TPPs) were fabricated. Figure 3.7 presents the process flow of TPP fabrication. Different from previously fabricated SiN_x nanopores in a standard Si wafer, TPP fabrication started with a double side polished silicon on insulator (SOI) wafer consisting of a 55 nm thick p-type Si layer and a 145 nm thick buried oxide (BOX) layer on a 300 μm thick silicon substrate. A 40 nm thick SiN_x layer was deposited on both sides of the SOI wafer by means of LPCVD. Circular nanoholes were then opened in SiN_x on the front side by combining EBL with RIE. After this, large cavities were etched on the rear side of the wafer with alignment to the nanoholes on the front side using photolithography in combination with DRIE and 30 wt% KOH etching in 80 °C. During the hot KOH etching, the front side of the wafer can be protected by the combination of a wet processing chuck and a protective coating layer (AR-PC 503, Allresist GmbH), as seen in Figure 3.8. The BOX serves as an excellent etch

stop layer (KOH etch rate of SiO_2 : Si =1:200). Compared with the etch rate of silicon in 30 wt% KOH at 80 °C around 1 $\mu\text{m}/\text{min}$ along $\langle 100 \rangle$ direction, the etch rate of silicon in 30 wt% KOH at 30 °C is around 30 nm/min along $\langle 100 \rangle$ direction. Therefore, 30 wt% KOH at 30 °C was then used to etch the top silicon in the SiN_x pore with a much more controllable manner. The protective coating layer can be stripped by a piranha cleaning ($\text{H}_2\text{SO}_4\text{:H}_2\text{O}_2 = 3\text{:}1$ vol.). After removal of the BOX in the large cavities, TPPs in free-standing silicon membranes were obtained.

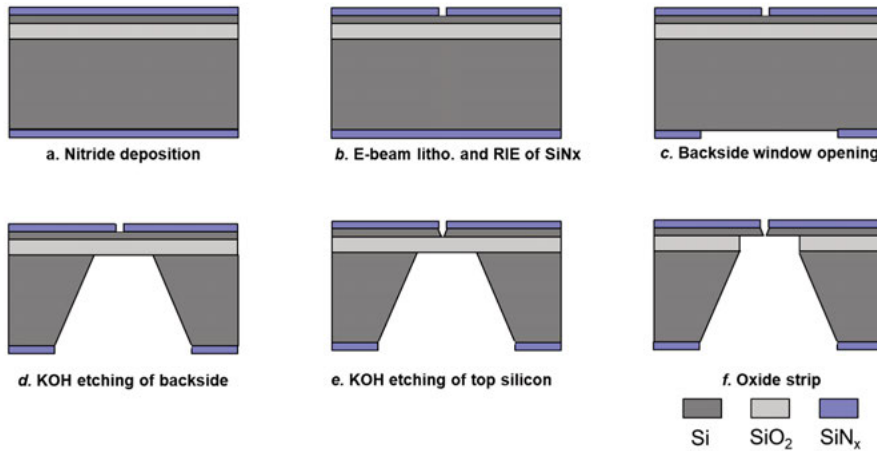


Figure 3.7. Schematic illustration of the fabrication process of TPP by wet chemical etching.

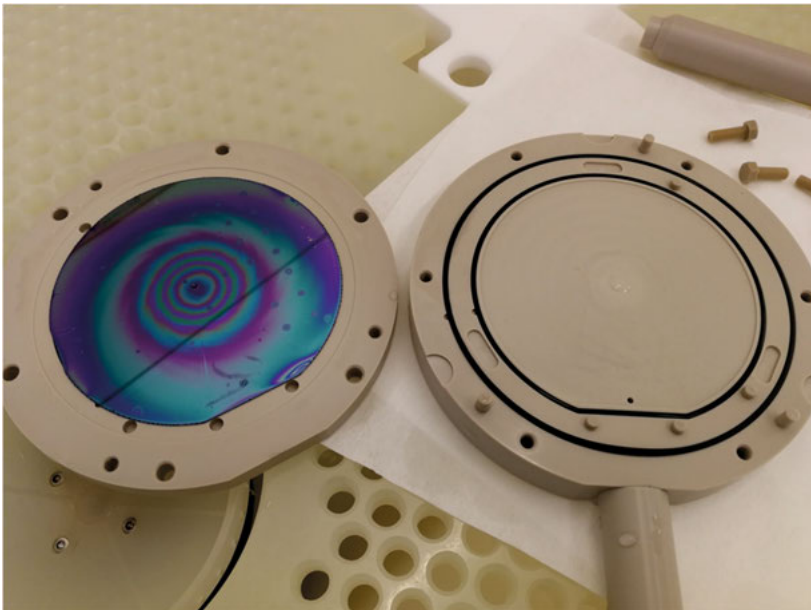


Figure 3.8. Protection of the front side of the wafer by combination of a wet processing chuck and a protective coating layer

The cross-section of the fabricated TPPs provides a direct observation of the size as well as the geometry of the TPPs. In order to obtain a good cross-section of the TPPs, a specially designed pattern with ultrahigh pore density of various sizes was prepared in the SiN_x mask layer, as shown in Figure 3.9. A set of cross-sectional SEM images of the fabricated TPPs with various sizes ranging from sub-5 nm to 60 nm are shown in Figure 3.10. These images were acquired with the bulk silicon substrate and BOX intact.

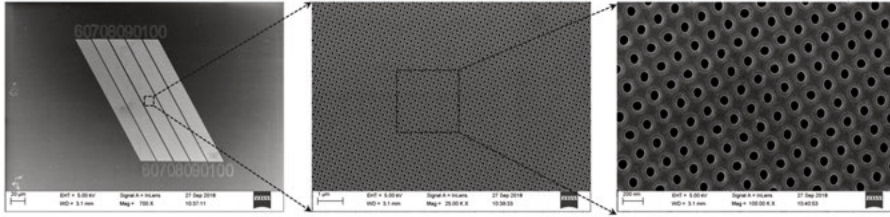


Figure 3.9. SEM images of specially designed pattern with ultra high pore densities of various sizes for cross-section evaluation.

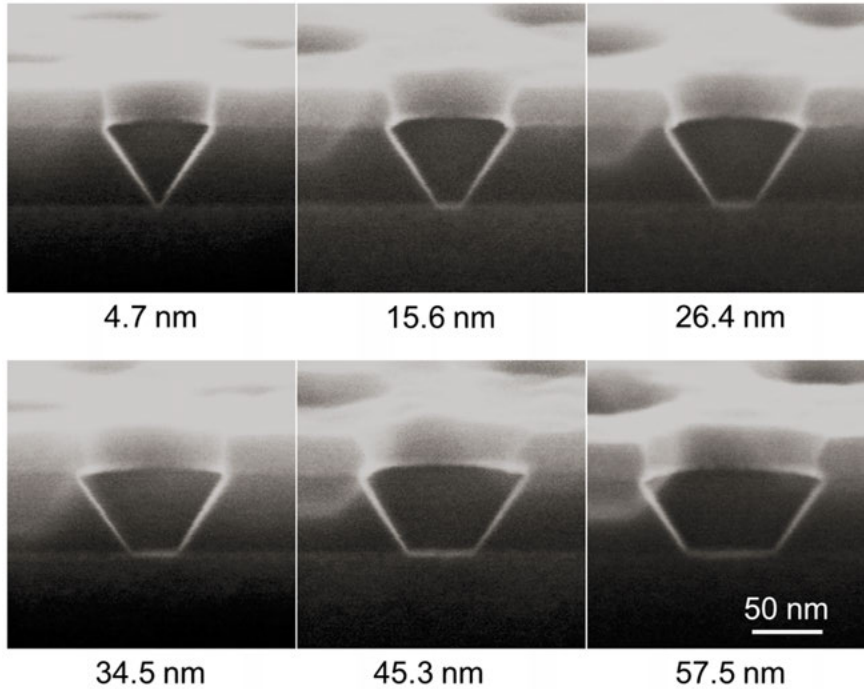


Figure 3.10. Cross-sectional SEM images of TPP ranging from 4.7 nm to 57.5 nm.

Figure 3.11 shows a set of TEM images of the fabricated TPPs with various sizes from 15 nm to 80 nm. Rectangular shape of the TPP instead of square is caused by the elliptical shape of the SiN_x mask patterned by EBL as a result of the deflection of the electron beam from the optical axis during writing the pattern. It is noteworthy to mention that the edges of TPPs are not as straight

as expected. A plausible explanation is that native oxide formed irregularly when the silicon becomes extremely thin and etched during BOX removal in BHF solution. With optimized experimental conditions, square shaped TPPs can be obtained, as shown in Figure 3.12. In Figure 3.12(a), the masking SiN_x layer was partially removed to contrast the silicon membrane with the TPP. By means of image greyscale analysis, the size of this TPP was measured to be 8 nm. Figure 3.12(b) shows a TEM image of an 8 nm TPP with high resolution. It can be seen that the pore tends to be circular shape. From Figure 3.12(c), undercut of the (111) planes can be clearly seen and this results in larger TPP size than desired dimension. Though there is very good selectivity between silicon (111) plane and (100) plane, KOH etching time of the top silicon layer also needs to be well controlled to reduce the (111) plane etching.

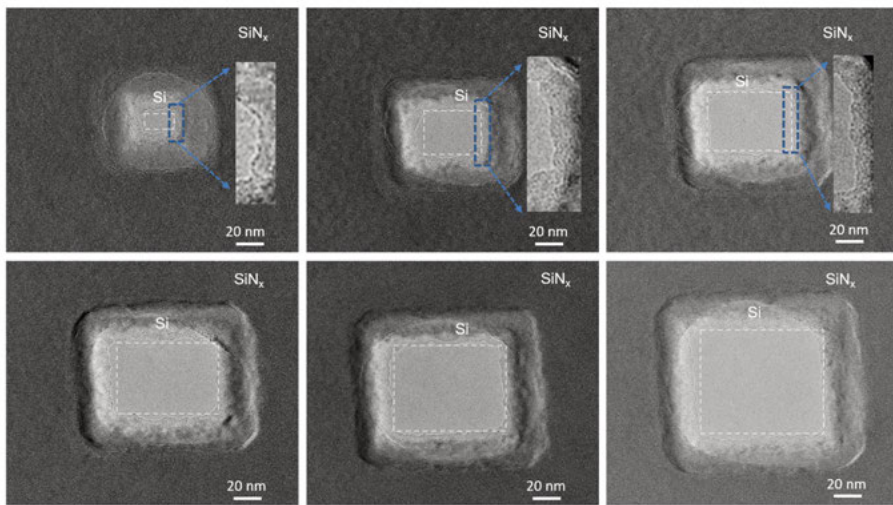


Figure 3. 11. TEM images of TPPs ranging from 15 nm to 80 nm. The dashed rectangle denotes the opened area of the pore. The insets in the top three images show close-up views of the rough edges of the corresponding images.

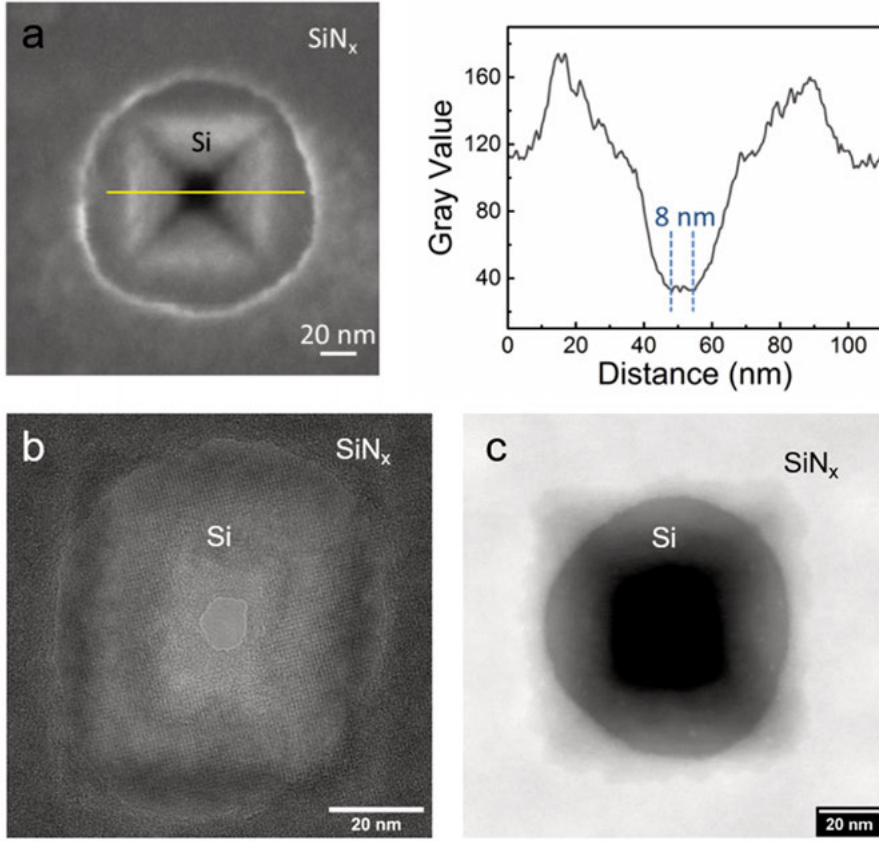


Figure 3. 12. (a) SEM image of an 8 nm TPP. (b) TEM image of an 8 nm TPP. (c) STEM image of an 30 nm TPP.

Before performing ionic current measurements, the electrical characteristics of the TPPs were firstly studied by numerical COMSOL simulations and our previously proposed physical model [58]. As seen in Figure 3.13(a), for a 20 nm conical shaped nanopore in a 55 nm-thick membrane with the angle of 54.7°, which is analogous to our fabricated TPPs, the electric field is most concentrated around the pore opening. The high electric field region (*i.e.* the effective length L_{eff}) is much shorter than the physical thickness of the membrane. Smaller L_{eff} implies a shorter region that is more sensitive to the obstruction by the analytes to be detected. Further on, the effective thickness of the conventional square column nanopores and SOI nanopores with different side length a and membrane thickness h were simulated and plotted in Figure 3.13(b). For conventional square column nanopores, L_{eff} increases linearly versus pore side length at different membrane thickness. However, for TPPs, L_{eff} shows a turning point where L_{eff} equals to membrane thickness but overall is much smaller than that of conventional pores. They show obvious advantages over conventional nanopores with high sensitivity.

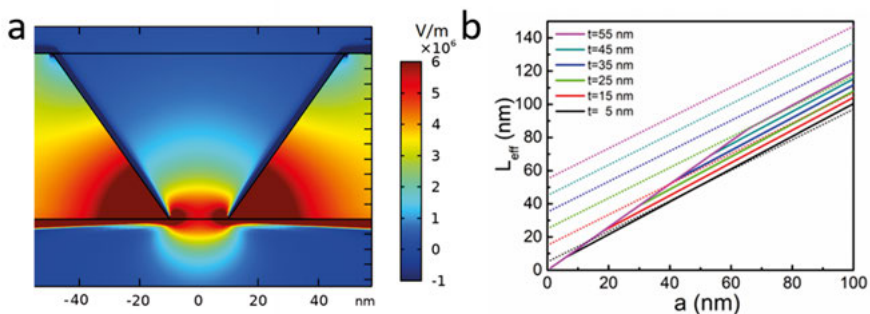


Figure 3. 13. (a) The electric field distribution of a conical shape nanopore simulated by COMSOL. The white lines represent electrical lines. The diameter of pore is 20 nm in a 55 nm-thick membrane with the angle of 54.7° and -0.02 C/m² surface charge. The simulation is taken in 100 mM KCl electrolyte at 0.2 V bias voltage. (b) Comparison of the effective length of traditional square column shape nanopores and TPPs with different side length a and membrane thickness t . The solid lines are for SOI nanopores, while the dotted lines are for square column shape nanopores.

3.5 Nanopore size reduction by electron beam induced carbon deposition (EBICD)

EBICD is often considered detrimental during SEM or TEM imaging since the deposited carbon can affect the resolution and contrast of an image [105], [106]. But EBICD process can also be used in many applications, such as acting as a mask for ion milling [107], welding nanostructures together [108], building complex nanostructures [109], as well as reducing the size of pre-fabricated nanopores [110]–[112]. We have explored a controllable method, using the EBICD process in a SEM, for the size reduction of pre-fabricated nanopores in free-standing SiN_x membranes. Successive size reduction of a nanopore of initial diameter 130 nm was monitored in real time during the first 15 min exposed to the electron beam at 5 kV and imaged with 200 K \times magnification (Figure 3.14(a)). The exact composition of the shrink layer (*i.e.* newly formed layer under the irradiation of electron beam) was confirmed by energy dispersive x-ray spectroscopy (EDX) mapping for a 130 nm SiN_x pore at its initial, partially closed and fully closed state, as shown in Figure 3.14(b). It was found that the shrink layer was predominantly composed of carbon with trace amount of oxygen.

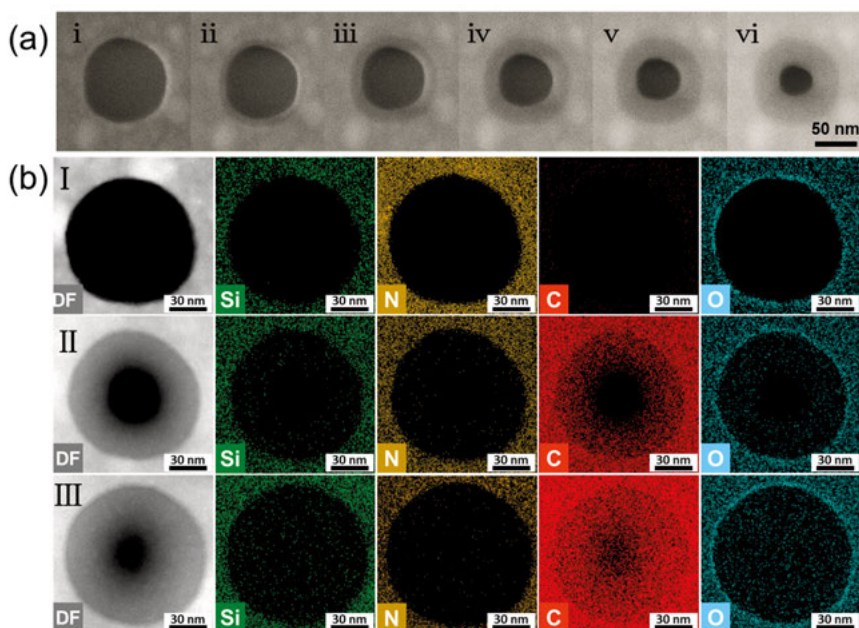


Figure 3. 14. Real time SEM images of the size reduction process as well as STEM dark field images and EDX mapping images. (a) Continuous size reduction of a 100 nm in the SiN_x membrane under the SEM from 0 min to 15 min with an increment of 3 min. (b) STEM dark field images along with EDX mapping images of an (I) initial, (II) partially size reduced and (III) fully closed 130 nm SiN_x pore. Adapted with permission from [113]. Copyright (2019) IOP Publishing Ltd.

There are several sources of hydrocarbon compounds present in the SEM system for EBICD: Organic contamination in the SEM chamber, adsorbed molecules on the sample surface and conductive carbon tabs used for stabilizing the sample on the SEM stub. By performing a control experiment without and with carbon tabs (Figure 3.15(a, b)), hydrocarbon molecules evaporated from the carbon tab (mainly acrylic acid) under the irradiation of electron beam transmitted through the SiN_x membrane was found to provide a stable source for EBICD. Acrylic acid, which is the adhesive in carbon tabs, has indeed been reported in the literature as a carbon precursor for the deposition of carbon [114]. A schematic illustration of the pore size reduction in SEM with the chip mounted on an adhesive carbon tab is presented in Figure 3.15(c), which can be explained as follows. As the electron beam irradiated the sample, most of the electrons would transmit through the thin SiN_x membrane and hit the conductive carbon tab, leading to the evaporation of hydrocarbon molecules. Some hydrocarbon molecules deposited and then dissociated around the nanopore under electron beam irradiation. The deposited carbon in turn reduced the size of original nanopores.

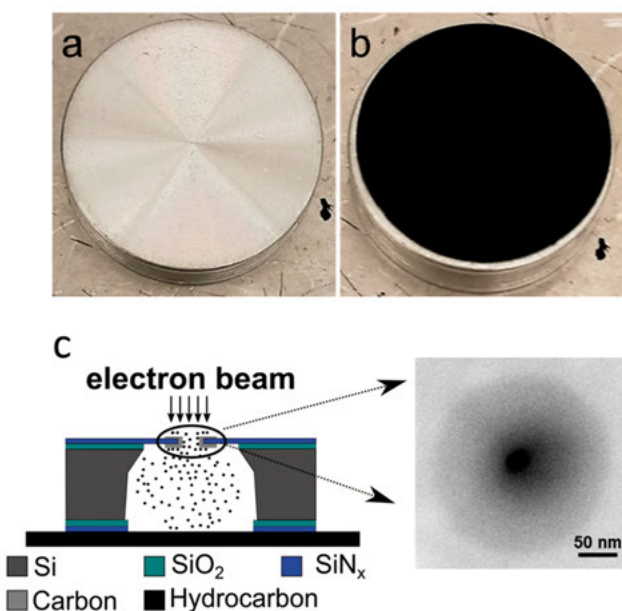


Figure 3. 15. Optical images of the SEM stubs without (a) and with (b) carbon tab as well as (c) schematic illustration of the pore size reduction in SEM with the chip mounted on an adhesive carbon tab.

More evidence to determine the dominant hydrocarbon source is provided in Figure 3.16 where the SEM cross section image shows a much thicker deposited carbon on the bottom part of the membrane than on the top. It is a natural outcome of hydrocarbon molecules being only evaporated from the carbon tabs below the pore. The deposited carbon near the nanopore is found to be thicker than the rest of the surface, which will be discussed in the following text.

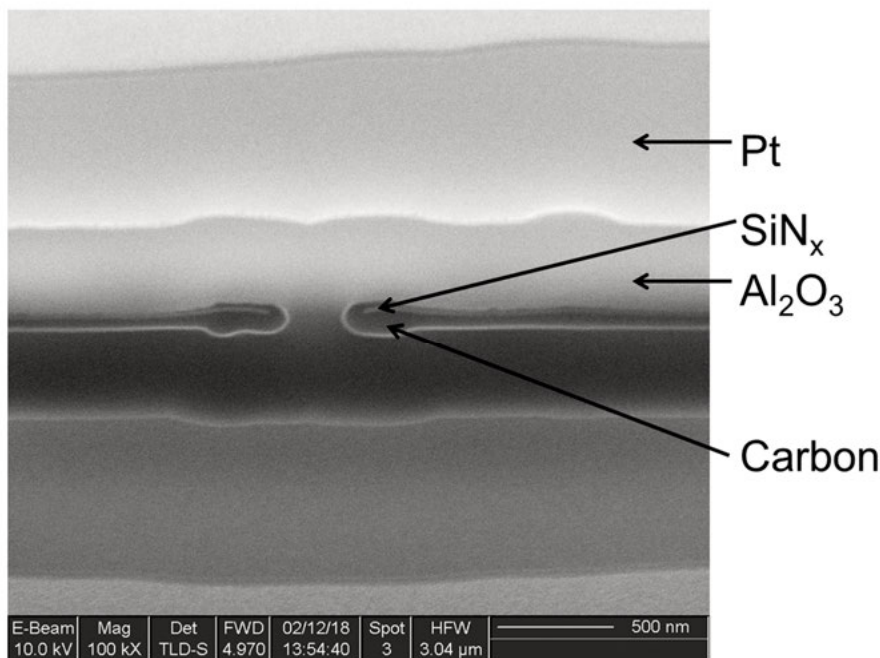


Figure 3. 16. SEM image of the cross section of a SiN_x nanopore after size reduction from 430 to 300 nm. The image is taken at a tilted angle of 52°.

Besides, different experimental parameters including electron beam parameters and membrane compositions were observed to affect the size reduction, as shown in Figure 3.17. For pores of initial diameter ranging from 130 to 800 nm under the electron beam irradiation at 5 kV and 200 K \times , the size reduction rate stayed constant at $0.090 \pm 0.022 \text{ nm s}^{-1}$. The rate was also found to linearly increase as the imaging magnification increased, since higher magnification implies higher electron flux. Moreover, the beam accelerating voltage played an important role of EBICD process. As seen in Figure 3.17(c), the pore size kept almost no change at 2 kV (*i.e.* 0.0072 nm s^{-1}) and the rate jumped to 0.16 nm s^{-1} at 5 kV. But as the beam voltage increased to 10 kV and 15 kV, the rate fell slightly back to 0.14 nm s^{-1} . Figure 3.17(d) shows that the rate of size reduction is sensitive to the choice of membrane material. For the samples with the SiN_x layer coated with TiN, TiO₂ and Al₂O₃ by atomic layer deposition (ALD), the rate behaved differently compared with the rate for the pore in SiN_x membrane. The rate dependence on accelerating voltage and material composition will be discussed in the following text.

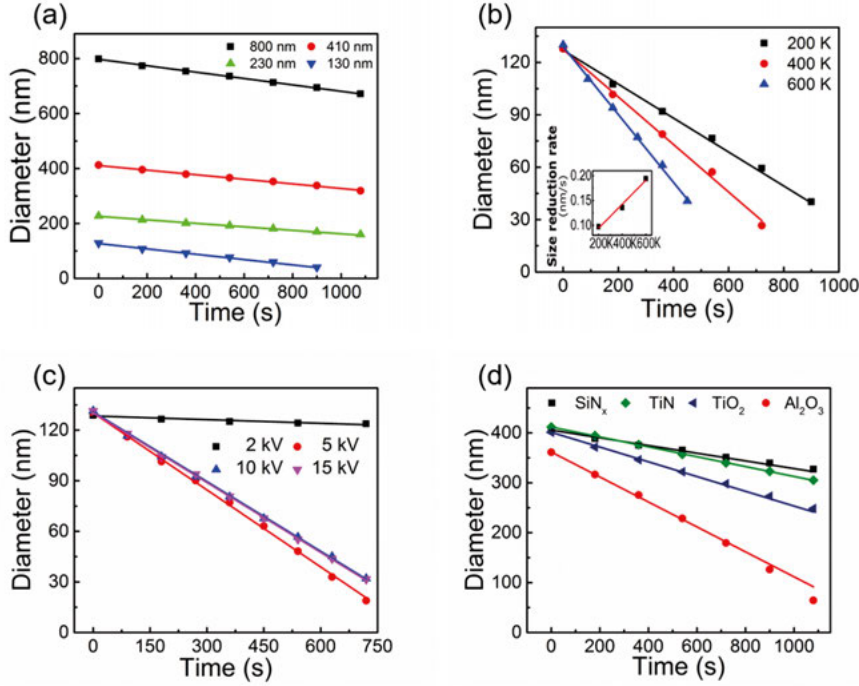


Figure 3.17. Dependence of pore size reduction rate on (a) initial pore size, (b) imaging magnification, (c) electron beam accelerating voltage and (d) ALD coating materials on the SiN_x layer. Adapted with permission from [113]. Copyright (2019) IOP Publishing Ltd.

The size reduction of pores is caused by carbon growth as a result of dissociation of adsorbed hydrocarbon molecules under electron beam irradiation. The growth rate R of the carbon layer follows the relationship below [115]:

$$R = vn\sigma f \quad (3.2)$$

where v [cm³] is volume per dissociated molecule, n [cm⁻²] surface concentration of adsorbates, σ [cm²] dissociation cross section of the adsorbed molecules under electron irradiation, depending on the beam energy and chemical composition of the adsorbate, and f [cm⁻².sec⁻¹] electron flux, including primary, backscattered and secondary electrons (PE, BSE and SE, respectively). So the pore size reduction rate is also influenced by these parameters: n , σ and f , and the results shown in Figure 3.17 can be explained in what follows. Firstly, the size reduction rate should be independent of the initial pore size, which is not included in Equation (3.2). Secondly, n can be regarded constant at each spot on the sample surface to be scanned over by the primary electron beam. This assumption is justified by the fact that the time duration for the irradiation of each spot was only less than 10 μ s whereas the total time of the exposure cycle was 732 ms. The adsorbate concentration can restore to the same level by the continuously arrived adsorbates on the surface. Thirdly, both

σ and f are highly dependent on electron energy. Although all electrons including PE; BSE and SE contribute to the carbon growth, SE of energy below 50 eV are considered to be dominant in this process because hydrocarbon molecules have much larger σ for electrons of lower energy [116]. Since each point along the original SiN_x pore rim should contribute to the total flux to the central plane and any point of that plane should on average receive the same amount of SE, the constant flux of SE implies the constant growth rate of the carbon layer. Higher flux of SE in the pore than the rest of the surface leads to thicker deposited carbon in the pore area. From the discussion above, the results shown in Figure 3.17(c-d) can be explained by SE flux change at various conditions. To verify the assumption, Monte Carlo simulations were performed using the CASINO modeling software to study the SE yield [117]. As shown in Figure 3.18, the trends of SE yield in different (a) accelerating voltage and (b) material compositions are consistent with those for the size reduction in Figure 3.17(c-d).

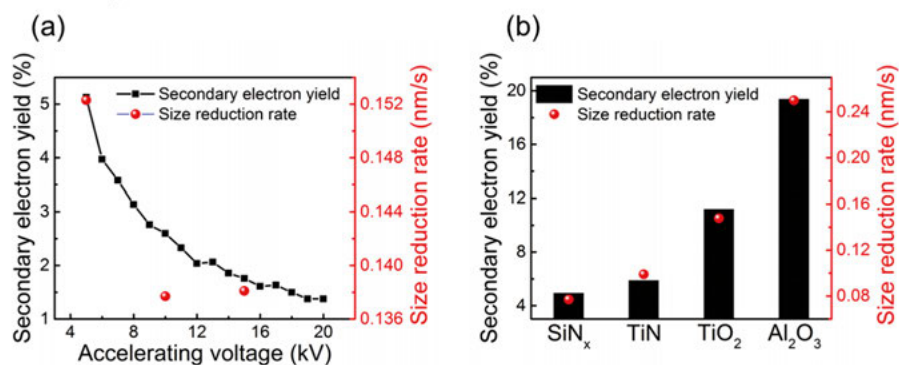


Figure 3.18. Casino Monte Carlo simulation of SE yield and size reduction rate at different accelerating voltage (a) and in different materials (b). Adapted with permission from [113]. Copyright (2019) IOP Publishing Ltd.

3.6 Nanopore size reduction by lipid bilayer coating

A well-controlled nanopore surface chemistry can not only improve sensing selectivity but also affect the non-specific interactions of analytes with the pores. Lipid bilayers, which are self-assemble dynamic biomimetic structures, provide a biologically relevant and well-defined coating of the nanopore surface [118]. Besides, the diameter of the nanopores can also be reduced by the lipid bilayer coating. Lipid bilayer thickness can be fine-tuned by the acyl-chain length and number of double bonds of the hydrocarbon tails of the lipids [48], [119]. The thickness of a POPC lipid bilayer is around 3.9 nm [120], and in addition an interstitial water layer of the thickness of 1.2 nm [48] is trapped between the bilayer and the support. As a consequence of lipid bilayer coating,

the nanopore size can be reduced by around 10 nm. An example of I - V characteristics of an 18 nm TPP before and after POPC lipid bilayer coating is shown in Figure 3.19(a). The diameter of the TPP after lipid bilayer coating is calculated to be 7.2 nm based on Equation (2.4) and (2.5), which matches the aforementioned discussion. It is noteworthy that a strong rectifying behavior is seen for the I - V characteristics of the bare TPP and the rectifying behavior is weakened after lipid bilayer coating. The weakened rectifying behavior is due to the almost neutrally charged condition of the POPC lipid bilayer. Figure 3.19(b) gives a comparison the noise PSD at various applied biases before and after lipid bilayer coating. It was claimed in the literature that the noise of a lipid bilayer coated SiN_x nanopore at low frequencies (<2 kHz) increases due to the dynamic motions with a supported lipid bilayer formed inside the nanopores [48], [121]. However, after lipid bilayer coating, the nanopore size is reduced and ionic current is also lower, which can result in lower PSD in the low frequency regime (see Equation (2.1) that PSD is a function of I^2 for flicker noise). So the overall PSD is a combined effect of both dynamic motions of lipid bilayer and reduction of ionic current. It can be clearly seen from our results that in the low frequency range, the PSD of the lipid bilayer coated TPP is overall lower than that of a bare TPP. This can possibly arise from the different pore material (SiN_x vs Si) as well.

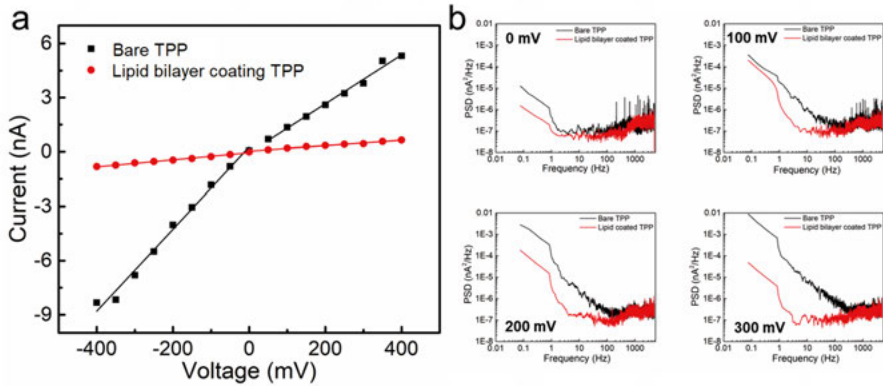


Figure 3. 19. I - V characteristics of an 18 nm TPP before and after POPC lipid bilayer coating (a) and a comparison of the noise PSD at various applied bias before and after lipid bilayer coating (b).

4. Sensing applications with single nanopores

In this chapter, I will present several sensing applications developed within this thesis framework using single solid-state nanopores. Both size reduced (by EBICD) SiN_x nanopores and Si TPPs are adopted to perform such tasks. Successful translocation of nanoparticles (**Paper II and IV**), DNA and protein (**Paper III**) is demonstrated. Besides, TPPs have also been used to provide a platform of studying the enzymatic reaction.

4.1 Nanoparticle translocation through a SiN_x nanopore with its size reduced by EBICD

After reducing the size of a SiN_x pore from 230 nm to 25 nm, its sensing capability was demonstrated with the electric detection of translocation of 20 nm silica nanoparticles. Firstly, the I-V characteristic in the open pore condition was measured by applying voltage from -1000 to 1000 mV in steps of 100 mV in a 100 mM KCl solution, as shown in Figure 4.1(a). Distinct conductance at positive and negative voltage range can be seen. The slight rectifying behavior could be caused by the asymmetric shape of the pore (see Figure 3.15) and/or non-uniform charge distribution along the sidewall of the pore. Although deposited carbon is considered to be hydrophobic, a treatment of piranha cleaning and oxygen plasma can activate the surface, make it hydrophilic and allow for conducting current-voltage measurements in electrolytes. Figure 4.1(b) depicts the representative ionic current traces of the translocation of silica nanoparticles through the size reduced pore. Several examples of the translocation events are given in Figure 4.1(c). There are mainly three types of blockade events found in the current traces. The long duration of type I event can be caused by a cluster of agglomerated nanoparticles. Type III represents the single-nanoparticle translocation event. The widened spikes in type II can possibly be caused by a weak interaction between the nanoparticle and the surface of the nanopore. Similar results are also found in Ref [122].

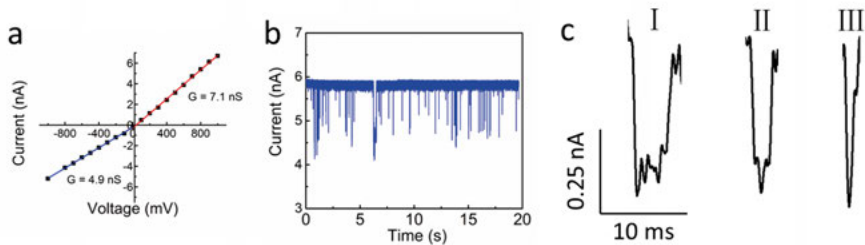


Figure 4.1. Electrical detection of 20 nm silica nanoparticle translocation through the nanopore. (a) I-V characteristic with 100 mM KCl solution. (b) Continuous current trace of blockage events. (c) Several examples of the detailed translocation events.

Statistical analysis of the translocation events was further performed. Figure 4.2(a) shows the distribution of the average amplitude and duration of all the translocation events along with the histograms for these two parameters. To further characterize the nanoparticle translocation, various biases ranging from 50 mV to 200 mV were applied. It can be seen in Figure 4.2(b, c) that the blockage amplitude increases and the duration time decreases as the applied bias increases. But for the translocation event frequency shown in Figure 4.2(d), it starts to increase from 50 mV to 100 mV and then becomes unchanged at 200 mV. The reason for this can be that the low pass filter is set at 1 kHz for this study and the translocation events are too fast to be detected at the high applied voltage. Overall, these results indicate that the size reduced nanopores by EBICD are comparable to their counterparts fabricated by other techniques [123], [124] in terms of sensing nanoparticle translocation.

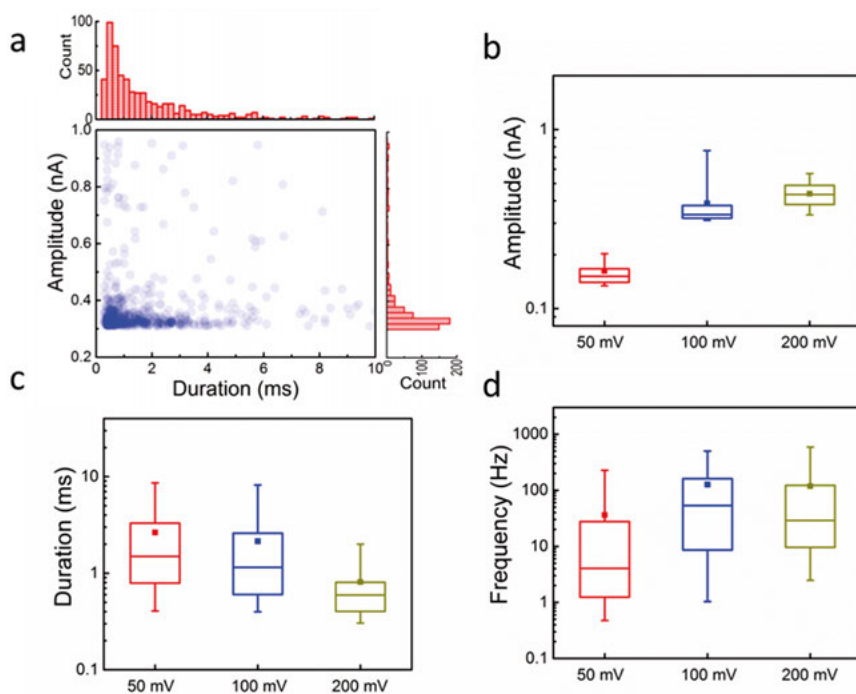


Figure 4.2. Statistical analysis of translocation events at different applied voltage. (a) Frequency distribution of the duration and amplitude of the observed current blockage. (b) Box plot of translocation event amplitude at 50 mV, 100 mV and 150 mV, respectively. (c) Box plot of translocation event duration at 50 mV, 100 mV and 150 mV, respectively. (d) Box plot of translocation event frequency at 50 mV, 100 mV and 150 mV, respectively.

4.2 DNA translocation through TPPs

λ -DNA translocation experiments were firstly performed to demonstrate the sensing capability of the fabricated TPPs. λ -DNA is in duplex structure and contains 48,502 base pairs. It is around 16 μm in length, but it takes a randomly coiled conformation in the electrolyte and the radius of gyration is estimated to be around 550 nm [125]. An 8 nm TPP was used for the experiment and λ -DNA was dispersed in a 10 mM Tris-HCl and 1 mM EDTA buffer (pH = 8.0) with a concentration of 78 pM. Figure 4.3(a) shows the typical ionic current trace of the translocation events. Figure 4.3(b, c) presents the box plots of both amplitude and frequency of translocation event at various bias from 300 mV to 800 mV with a step of 100 mV, respectively. As can be clearly seen, both the amplitude and frequency increase as the applied bias increases.

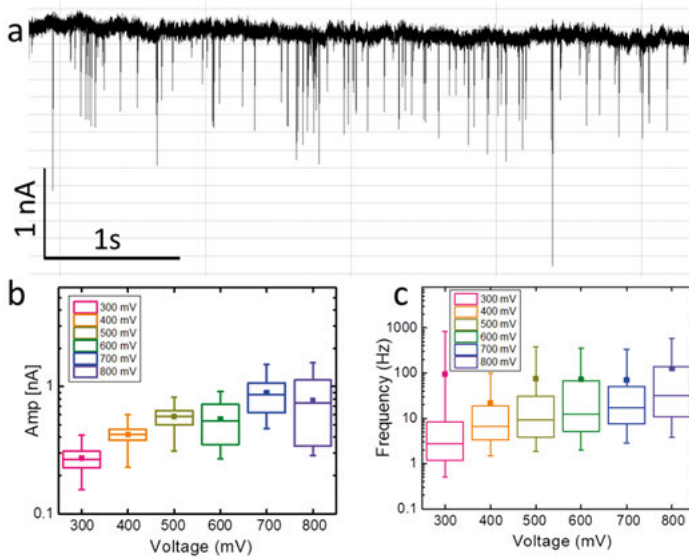


Figure 4.3. (a) Ionic current traces of λ -DNA translocation through an 8 nm TPP and statistical analysis of translocation events at different applied voltage. (b) Box plot of translocation event amplitude at various bias from 300 mV to 800 mV with a step of 100 mV, respectively. (c) Box plot of translocation event frequency at various bias from 300 mV to 800 mV with a step of 100 mV, respectively.

4.3 Protein translocation through TPPs

Apart from λ -DNA, proteins have also been used for demonstration of the sensing functionality of the TPPs. Two representative proteins were chosen: disc-like IgG₁ of 15 nm in diameter and 8 nm in thickness and sphere-like streptavidin of diameter 6 nm [33]. By only adding streptavidin to the upper side of the TPP, the translocation of streptavidin through the TPP only occurred at a positive bias, as shown in Figure 4.4. The point of isoelectric (pI) is around 5 for streptavidin. Therefore, streptavidin is negatively charged at pH = 7.4. However, the translocation direction is opposite to that of the electrophoretic force. As discussed in Chapter 2, EOF mainly provides the driving force for streptavidin translocation. The dependency of mean frequency of translocation event (FTE) is shown in Figure 4.5(a, b) when a TPP of $a=18$ nm and a TPP of $a=10$ nm used for translocating streptavidin, respectively. For the TPP of $a=18$ nm FTE is higher and its increase with applied bias is steeper at positive bias in comparison to that at negative bias. But for the TPP of $a=10$ nm and FTE is low at positive bias, while it stays higher at negative bias. Similar trends are also found for the translocation of IgG₁ through a TPP of $a=73$ nm and a TPP of $a=18$ nm, respectively. The rectification in mean FTE is highlighted by summarizing the FTE ratio defined by

$Ratio = \frac{Mean FTE_{negative bias}}{Mean FTE_{positive bias}}$ in Figure 4.5(d) for all four cases. Size match between protein and pore dimension appears to play a decisive role.

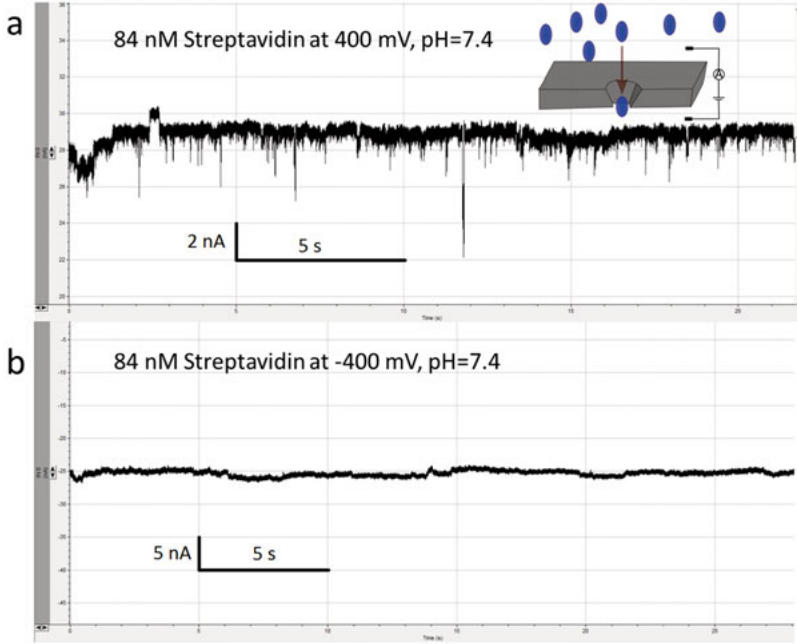


Figure 4.4. Ionic current traces of streptavidin translocation through an 18 nm TPP at pH=7.4 by applying a bias of 400 mV and -400 mV, respectively. The inset shows the schematic of the measurement setup and streptavidin was only added to the upper side of the TPP.

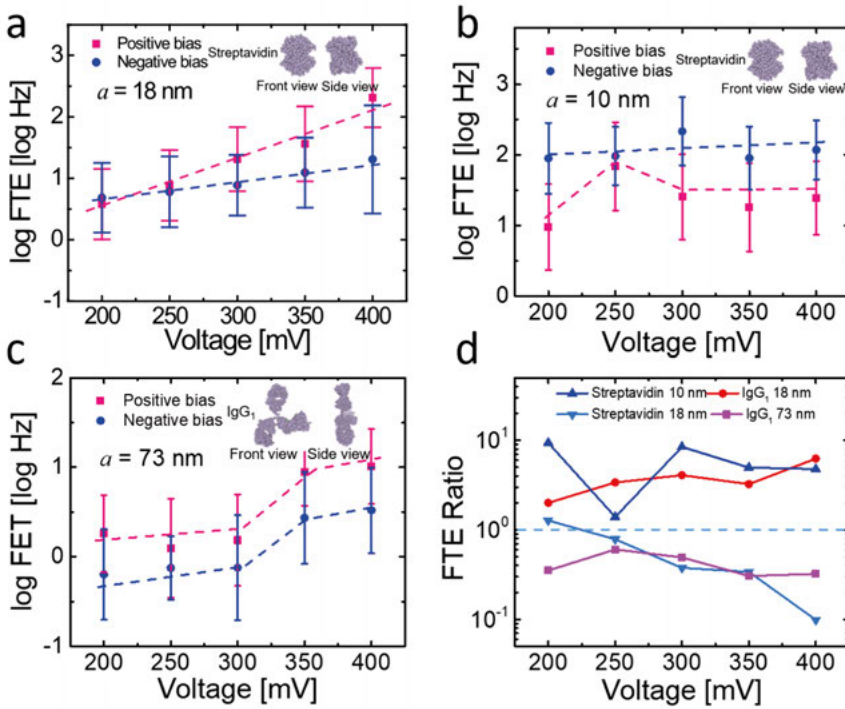


Figure 4.5. Mean FTE for streptavidin and IgG₁ in TPPs of different a . (a) Streptavidin in a TPP of $a=18$ nm. The insets show the three-dimensional conformation of streptavidin with atomic resolution from the Protein Data Bank. (b) Streptavidin in a smaller TPP of $a=10$ nm. (c) IgG₁ in a larger TPP of $a=73$ nm. The insets show the three-dimensional conformation of IgG₁ with atomic resolution from the Protein Data Bank. The error bars in (a-c) indicate the spreads of the distribution of corresponding statistic variables. (d) Ratio of mean FTE at negative bias to that at positive bias versus applied voltage. Size match between protein and pore dimension appears to play a decisive role.

From numerical simulations by employing COMSOL Multiphysics, an electroosmotic vortex is found to form inside the TPP, as shown in Figure 4.6(a). The vortex is easily visualized by mapping the electroosmotic flow velocity in Figure 5b for a positive bias at +200 mV and a negative bias at -200 mV. The vortex formation is due to the geometrical asymmetry of the nanopore and the charge distribution along the sidewalls of the nanopore. The flow direction inside the vortex is opposite that of the flow outside. It is obvious that the vortex is smaller and the gap between the vortex and the nanopore sidewall is larger when the nanopore is negatively biased (left halves in Figure 4.6(a)). Similar results of a reversed electroosmotic flow were also found for a pore in a SiN_x membrane under viscosity gradients [126]. Figure 4.6(b) shows that at

positive bias voltages, the electroosmotic flow is faster than that at the corresponding negative bias voltages.

Therefore, for cases where the size of the translocating molecules is comparable to or larger than the narrowest gap between the vortex and the nanopore sidewall of TPP, *i.e.*, IgG₁ translocation in the TPP of $a=18$ nm and streptavidin translocation in the TPP of $a=10$ nm, the vortex appears to act as a piston whose size and position can be controlled by applied voltage and surface

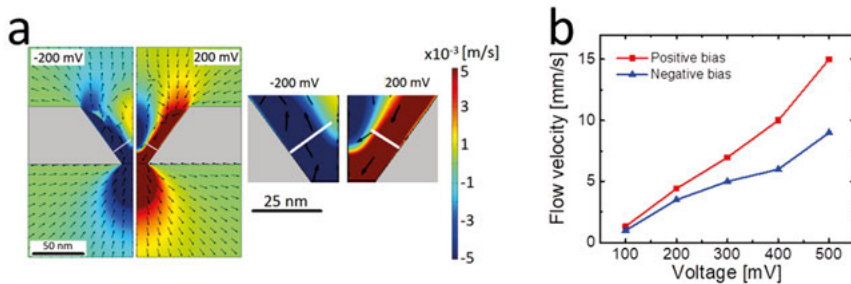
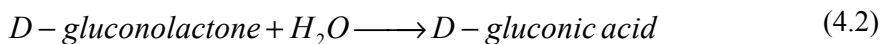
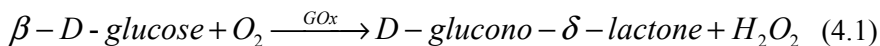


Figure 4.6. COMSOL simulations for a truncated conical nanopore, 20 nm in diameter of the bottom base, 55 nm in membrane thickness, and 54.7° for the sloped sidewall, in 100 mM KCl and with $\sigma=-0.02$ C/m². (a) Electroosmotic flow velocity distribution at -200 mV (left half) respective 200 mV (right half), left, and a close-up view of the narrowest gap region, right. Warm colours (red and yellow) indicate downward flows, while cold colours (blue and green) present upward flows. The small black arrows indicate the direction of the flow, from which a vortex is clearly visible in the centre of the pore. The smallest gap between the vortex and the nanopore sidewall is indicated by the short white lines. (b) Dependence of the average velocity of the electroosmotic flow in the narrowest gap on applied voltage.

4.4 Enzymatic reaction monitoring with TPPs

By making use of the asymmetric shape of the TPPs, a special experiment was designed to monitor the enzymatic reaction with TPP. Enzymes are loaded into a TPP and not able to translocate through the TPP due to size restriction. A local pH change generated by the enzymatic products is expected to modify the surface charge density of the sidewalls of TPP and thereby modulate the ionic current. Glucose oxidase (GOx) is chosen in the experiment. The enzymatic reactions of GOx in glucose solution can be listed below [127]:



As shown in Equation (4.1) and (4.2), a certain pH change of local environment is expected by the enzymatic oxidation of glucose to gluconic acid catalyzed by GOx in glucose solution. The native GOx size is around 8 nm [128], which requires an ultra small TPP with its size much smaller than 8 nm to be able to prevent the translocation of GOx through TPP. Therefore, GOx nanocapsules are prepared by forming a polymer network around GOx to increase their sizes to be around 23 nm. This has reduced the difficulty of TPP fabrication and 10 nm TPPs can be utilized for such a study. Figure 4.7 gives a schematic illustration of the measurement configuration for enzymatic reaction monitoring with a 10 nm TPP. GOx nanocapsules are added to the upper side of the TPP and glucose is then added to the lower side of the TPP. Nanocapsules are negatively charged and a bias can therefore be applied to load the nanocapsules into the TPP. The interior of TPP is the only position where GOx can be in contact with glucose and the enzymatic reaction occurs.

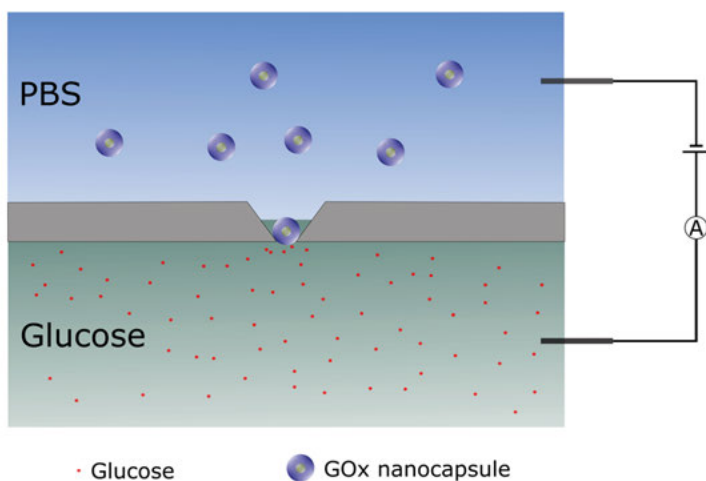


Figure 4.7. Schematic of measurement configuration for enzymatic reaction monitoring with a TPP. The glucose oxidase nanocapsules with the diameter around 23 nm are added into the upper side of the TPP and glucose is added into the lower side of the TPP. Therefore, the enzymatic reaction can only happen in the TPP where glucose oxidase meets the glucose.

As shown in Figure 4.8(a), the open pore current is firstly measured with both sides of TPP filled by $1\times$ PBS buffer solution at different applied bias from -400 mV to 400 mV with a step of 100 mV. Then the nanocapsules are added to the upper side of TPP and a positive bias is applied. TPP is blocked by the nanocapsule. The ionic current is measured again at different applied bias from -400 mV to 400 mV and a clear rectifying behavior can be seen. Glucose with a concentration of 0.005 M is added to the lower side of the TPP to initiate the enzymatic reaction. This is followed by another two experiments at glucose concentrations of 0.05 M and 0.2 M, respectively. By counting the

ratio of absolute value of the monitored ionic current at positive bias to that at negative bias versus applied voltage, as shown in Figure 4.8(b), different rectifying behaviors are obtained in different glucose concentrations. The ratio is around 1 for bare PBS solutions and becomes around 0.5 after adding GOx nanocapsules. As the glucose concentration increases, the enzymatic reaction rate also increases and more acidic products are produced, leading to an increase in the rectifying ratio. But this trend doesn't fully apply at high applied bias, the cause of which is unknown and further investigation needs to be performed.

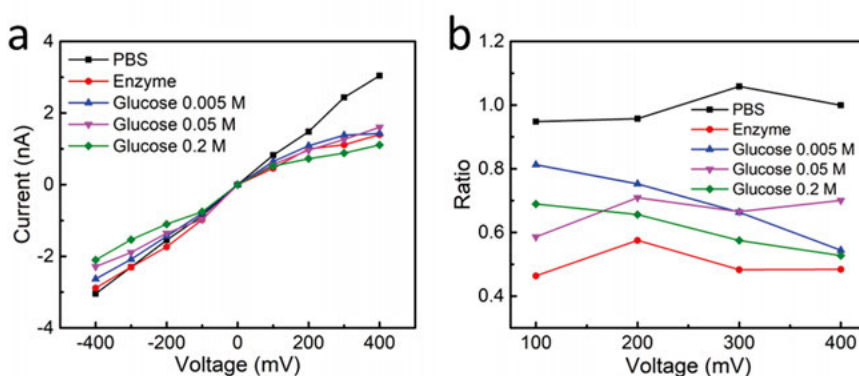


Figure 4.8. Electrical monitoring of enzymatic reaction with a 10 nm TPP at different glucose concentrations. (a) I-V characteristics in bare PBS, after adding enzyme and at different glucose concentrations. (b) Ratio of absolute value of the monitored ionic current at positive bias to that at negative bias versus applied voltage.

5. Sensing applications of nanopore array

Compared with single nanopores in sensing applications, nanopore arrays or multiple nanopores have the advantages of high throughput and parallelized sensing capability in measurement. In this chapter, several attempts with either nanopore array fabricated in a single free-standing membrane (**Paper II and V**) or multiple free-standing membranes with single nanopore on each (**Paper VI**) have been made for different applications.

5.1 Single free-standing membrane with multiple nanopores

5.1.1 SiN_x nanopore array for nanoparticle translocation

Nanopore arrays with different sizes and spacing between two adjacent pores can be easily defined and massively produced by making use of EBL and RIE. Figure 5.1 shows a set of SEM images of 400 nm pores in free-standing SiN_x membrane with various amounts from 1, 10, 30 to 100.

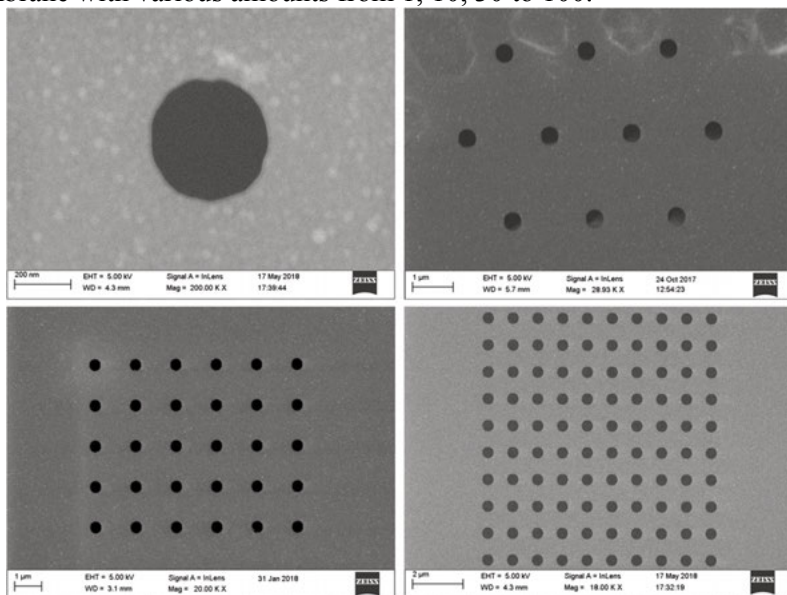


Figure 5.1. SEM images of 400 nm pores in free-standing SiN_x membrane with various amounts from 1, 10, 30 to 100.

For multiple pores in a free-standing membrane, the output ionic current is a superposition of the ionic currents from all the pores in the membrane simultaneously. In this study, the translocation of 30 nM silica nanoparticles of 160 nm in diameter through 400 nm SiN_x pores with various amounts N was performed. The number of pores on a device was increased successively from 1 to 10 for this set of experiments. As shown in Figure 5.2(a), current spikes induced by the translocation of silica nanoparticles become increasingly difficult to distinguish as the number of pores increases. In order to show the details of the waveform of the current traces, respective average current values are subtracted for the traces displayed in Figure 5.2(a). The PSD of these current traces were calculated and shown in Figure 5.2(b). From the PSD curves, it can be obviously seen that the current fluctuations increase with an increase in the pore amounts. Clear trends in average of the ionic current (I_{ave}) and its standard deviation (STD) versus the number of pores are also observed, as shown in Figure 5.2(c, d). I_{ave} increases linearly with the number of pores, which is a straightforward result of the summation of the ionic current of each individual pore, and STD follows a square root law versus the number of pores, which can be explained as follows. The randomly generated blockage spikes of the ionic current caused by the translocation of nanoparticles through a single pore resemble those of random telegraph noise (RTN) [129]. The PSD of the translocation waveform can thereby be written as:

$$S(f) = \frac{4\Delta I^2}{(\tau_o + \tau_b) \left[\left(\frac{1}{\tau_o} + \frac{1}{\tau_b} \right)^2 + (2\pi f)^2 \right]} \quad (5.1)$$

where ΔI is the amplitude of blockage caused by the translocation, τ_o and τ_b are mean dwell time of open pore state and blockage stage, respectively, and f is frequency.

For multiple pores, the total PSD is the summation of the PSD of each individual pore assuming that the translocation events at different pores are independent:

$$S_N(f) = \sum_{i=1}^N S_i(f) \quad (5.2)$$

Therefore, STD of the total current can be obtained by integrating the PSD over the entire frequency range:

$$STD = \sqrt{\int_0^\infty S_N(f) df} = \frac{\Delta I \sqrt{N\tau_o\tau_b}}{\tau_o + \tau_b} \quad (5.3)$$

I_{ave} can be calculated straightforwardly by averaging the current:

$$I_{ave} = N \frac{I_o \tau_o + (I_o - \Delta I) \tau_b}{\tau_o + \tau_b} \quad (5.4)$$

where I_o is the open pore current.

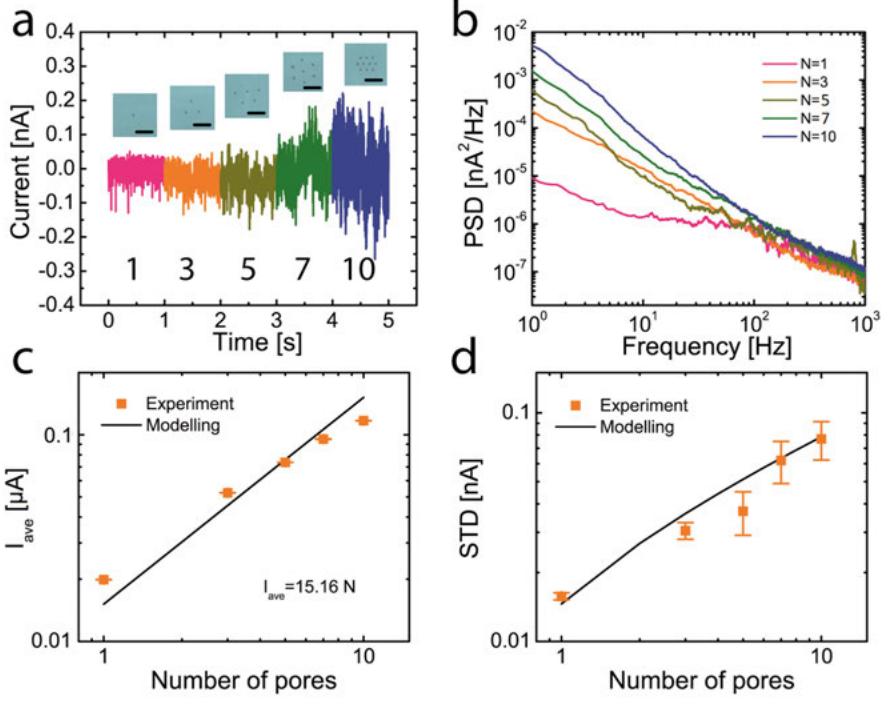


Figure 5.2. Experimental results of silica nanoparticle translocation by varying the numbers of nanopores in the free-standing SiN_x membrane. (a) Ionic current traces of 160 nm silica nanoparticles translocating through nanopores by increasing the pore amount from 1 to 10 at 200 mV. The inset shows optical micrographs of five devices with different amounts of pores. (b) PSD of ionic current for nanoparticle translocation through nanopores with different amounts. (c) Variation of I_{ave} as a function of pore amounts. (d) Variation of STD as a function of pore amounts. The error in (c, d) is standard deviation of six 1 s- current segments. Adapted with permission from [130]. Copyright (2019) American chemical Society.

The variations of I_{ave} and STD as a function of the concentration of nanoparticles at various applied biases are shown in Figure 5.3(a, b). It can be seen that I_{ave} increases with the increase of applied bias but decreases as the concentration of nanoparticles increases. STD behaves in a complex trend and a maximum shows up at a certain concentration. The maximum appears at lower concentrations at higher applied bias, indicating synergistic effects of applied bias and concentration. Both applied bias and concentration can affect the capture rate of nanoparticles and dwell time of translocation, thereby affecting τ_o and τ_b . Therefore, by analyzing the details of I_{ave} and STD , the concentration of nanoparticles can be inferred. Larger amounts of nanopores promise faster

measurements at lower concentrations of nanoparticles, as a result of larger capture cross sections for the target nanoparticles.

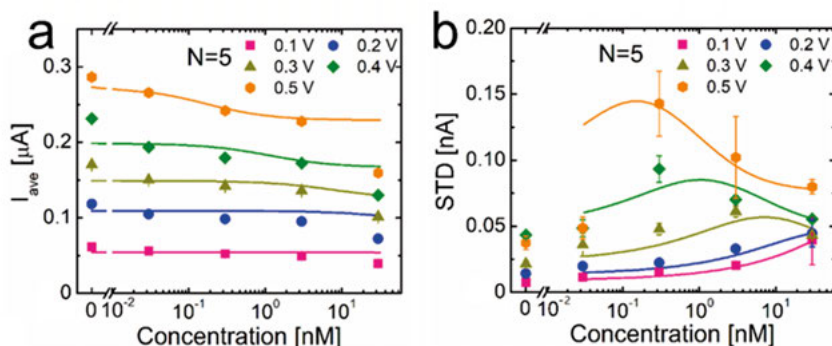


Figure 5.3. Experimental results using a five-pore device. (a) Variation of I_{ave} with a concentration of nanoparticles at different bias voltages. (b) Variation of STD with a concentration of nanoparticles at different bias voltages. Adapted with permission from [130]. Copyright (2019) American chemical Society.

5.1.2 TPP array for lipid bilayer formation

In this work, we used TPP arrays as the substrate for lipid bilayer formation. Figure 5.4(a) shows SEM images of a 5×5 TPP array with a pore spacing of 1 μm and the insets depict a higher magnification image of one of the pores as well as a cross-sectional view of the pore. Vesicles were added to both reservoirs sandwiching the TPP chip and a bias was then applied through the Ag/AgCl electrodes connected with the custom-made flow cell. Figure 5.4(b) presents a typical example of the monitored ionic current trace after adding vesicles with a hydrodynamic radius (R_H) of 92 nm at 50 mV. It can be clearly seen that the ionic current started to decrease step by step as the voltage was applied. The decrease was rapid in the beginning, then became slower and finally tended to level off. All the vesicles used were larger than the TPP and no vesicle translocations were expected.

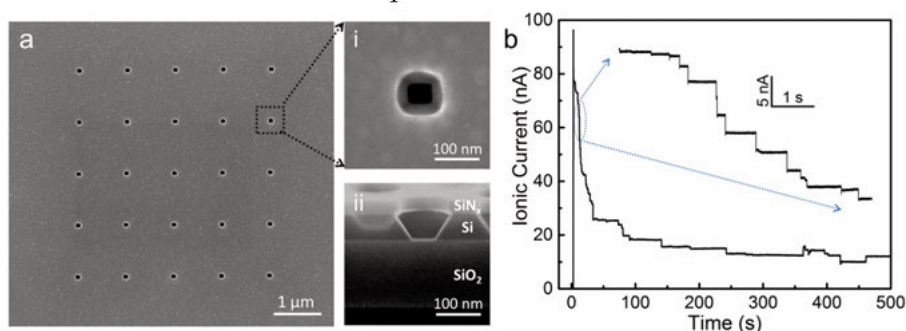


Figure 5.4. SEM images of a TPP array (a) and the measured ionic current trace through the TPP array at 50 mV after adding vesicles ($R_H = 92$ nm) (b).

Various parameters including applied bias, vesicle size and concentration were investigated how the monitored ionic current traces are affected. Assuming that the lipid bilayer is fully and uniformly formed inside the TPP thus reducing the TPP size by 10 nm, the ionic current drop per pore is calculated to be 0.27 nA at 20 mV, 0.71 nA at 50 mV and 1.30 nA at 100 mV. Taking this as unity at respective bias, the number of size reduced pores (N_{SRP}) can be calculated as current drops divided by unity, which can be used to normalize the current drops obtained in different experimental conditions. N_{SRP} can be used to characterize to which extent the interior of TPPs is covered by the lipid bilayer and non-integers can appear. If a TPP is fully blocked by the lipid bilayer, the resulting N_{SRP} should be much more than 1. Figure 5.5 shows the results of statistical analysis of current steps of the recorded ionic current trace in different conditions. As seen in Figure 5.5(a), current drop events appear intensely within the first 50 s after the bias was applied from 20 mV to 100 mV. The percentage of the events (*i.e.* current drops) within the first 50 s over the whole 500 s timespan (P_{50s}) increased from 41% to 68% when the bias was increased from 20 mV to 100 mV, as summarized in Table 5.1. This implies that higher bias accelerated the process leading to more rapid current drops. However, at different bias, N_{SRP} exhibited a similar distribution although the frequency (*i.e.* the ratio of the number of events for a certain N_{SRP} to the total number of events) was slightly different (see Figure 5.5(b)). N_{SRP} appeared most frequently at around 0.5, indicating that lipid bilayer only partially covered the interior of a TPP. Thus, the variations in N_{SRP} can be attributed to different partial coverages of the formed lipid bilayer in the TPPs. Only a small fraction of events show a large N_{SRP} value around 4. These events can be caused either by the blockage of TPPs or by the simultaneous formation of lipid bilayer in multiple pores. Figure 5.5(b) shows that the majority of events resulted in a N_{SRP} close to, or below 1, that is where we are mainly focused on. The value of N_{SRP} in the horizontal axis represents the extent that lipid bilayer covers the interior of TPP and the frequency in different conditions is not compared here.

Figure 5.5(c-d) shows the obtained results with vesicles of different sizes. Both P_{50s} and N_{SRP} increase as the vesicle size increases. Larger vesicles have higher capture cross section to adsorb in the TPPs, leading to a high P_{50s} , and larger surface area, resulting in a large N_{SRP} . As presented in Figure 5.5(e-f), an increase of P_{50s} was also seen as the vesicle concentration was increased from 0.04 nM to 0.4 nM. However, N_{SRP} appeared at almost the same position regardless of the lipid concentration owing to the fact that the vesicle size ($R_H = 92$ nm) was identical for all the concentrations.

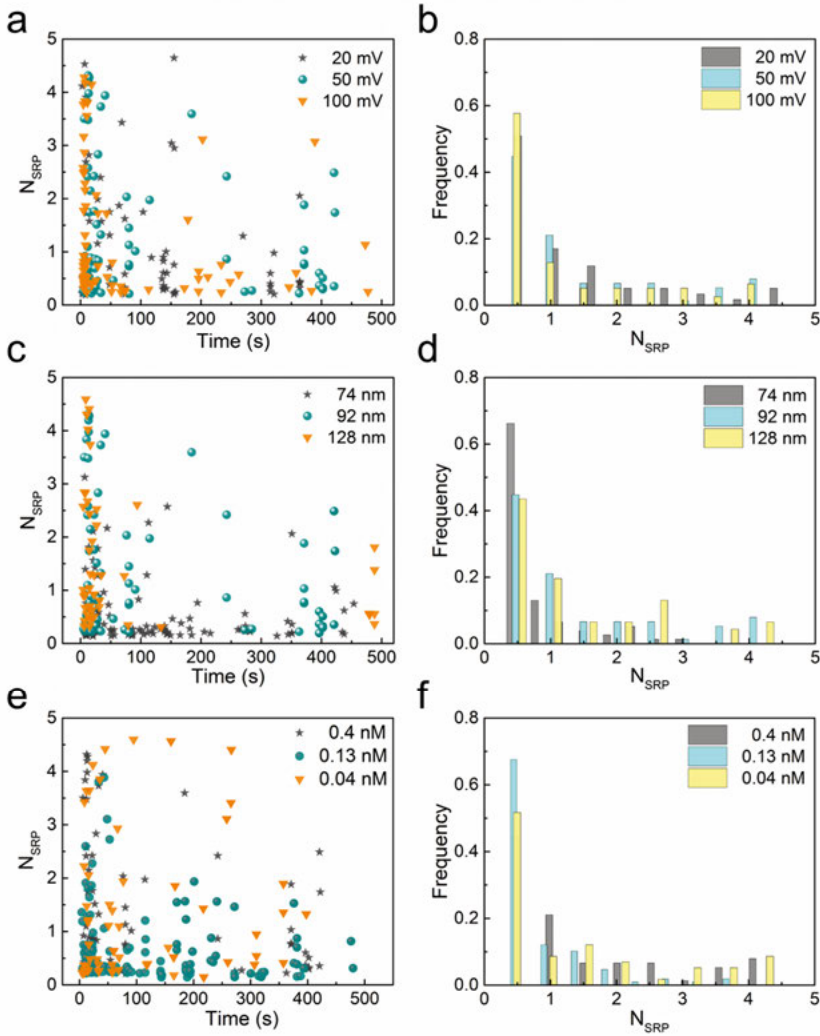


Figure 5.5. Statistical analysis of current steps of the recorded ionic current trace of 5×5 nanopore arrays at 50 mV by adding different sized vesicles. (a) N_{SRP} versus time at different applied bias. (b) Relative frequency of N_{SRP} at different applied bias. (c) N_{SRP} versus occurred time with vesicles of different sizes. (d) Frequency of N_{SRP} with vesicles of different sizes. (e) N_{SRP} versus occurred time with vesicles ($R_H = 92$ nm) at different concentrations. (f) Frequency of N_{SRP} with 92 nm vesicles at different concentrations.

Table 5.1. Percentage of events within first 50 s over the whole time span (P_{50s}) at different conditions.

Concentration (nM)	Vesicle radius (nm)	Applied bias (mV)	P_{50s} (%)
0.4	92	20	41
		50	63
		100	68
0.4	74	50	45
	92		63
	128		76
0.4	92	50	63
0.13			51
0.04			44

From the findings described above, the process of lipid bilayer formation in the TPPs can be inferred as follows: Vesicles diffuse to the TPPs, adsorb in the opening of the TPPs and rupture instantaneously to form the bilayer. Once a vesicle is in contact with a solid support, vesicle-solid contact creates a new interface and at the same time eliminates the original solid-liquid interface and vesicle-liquid interface. This new interface energy γ_{VS} can be lower than the sum of solid-liquid interface energy γ_{SL} and vesicle-liquid interface energy γ_{VL} . Therefore, the energy minimization caused by the new vesicle-solid interface formation can be the driving force for the vesicles' adsorption on the support surface. But the new vesicle-solid interface also causes some deformation of the vesicles, which can in turn increase the surface tension of vesicles. In the presence of TPPs, the truncated pyramidal shape of a TPP creates a larger vesicle-solid contact area than that of vesicle on a planar support. Increased contact area further deforms the vesicle which leads to an even higher surface tension. When the surface tension reaches a critical value, vesicles rupture to lipid bilayer. This could be a plausible explanation of the instant rupture of the vesicles in the TPPs.

TPPs act as active surface sites which can be adsorbed by vesicles and meanwhile visualized via ionic current monitoring. Vesicles can also adsorb on the rest of the surface other than TPPs and remain intact until they are in contact with the active edge of formed lipid bilayer or reaching a critical coverage, but this process cannot be monitored by ionic current. Current drops are caused by vesicle adsorption and subsequent rupture in TPPs. The overall trend of the current decrease can reflect the rate of vesicle adsorption on the

whole surface. The quicker vesicles absorb on the surface, the faster the current decreases. Therefore, the rate of the overall current decrease can be described as follows:

$$\frac{dI}{dt} = k(I - I_e) \quad (5.5)$$

After integration and applying boundary conditions, equation 5.5 becomes:

$$I_t = (I_0 - I_e)e^{-kt} + I_e \quad (5.6)$$

where I_e and I_t are the ionic current at equilibrium and at time t , I_0 is the open pore current, and k is the rate constant, which is related to vesicle size and concentration. However, the recorded time when lipid bilayer started is not exactly $t = 0$. Therefore, fitted values of I_e and I_t can deviate from the actual values, but the rate constant k remains unchanged no matter when the ionic current is recorded. Table 5.2 summarizes the extracted rate constant k from fitting the experimental results at different conditions. The dependence of k on the applied bias can be related to the increased EOF velocity at higher bias since POPC vesicles are electrically neutral in the solution and more vesicles will be taken to the vicinity of TPPs by EOF. Basically, EOF flow velocity increases as the applied bias increases, as discussed in our previous work [72]. The dependence of k on vesicle size can be explained in the same way as that of P_{50s} that larger vesicle has higher capture cross section to adsorb in the TPPs. The dependence of k on vesicle concentration is in consistency with the fact that more vesicles can reach the surface at higher concentration.

Table 5.2. Rate constant at different conditions with the ionic current trace fitted with Equation 5.2.

Concentration (nM)	Vesicle radius (nm)	Applied bias (mV)	Rate constant k (s^{-1})	Goodness of fit (R^2)
0.4	92	20	0.0089	0.95
		50	0.042	0.94
		100	0.24	0.96
0.4	92	50	0.020	0.96
			0.042	0.94
			0.10	0.95
0.4	92	50	0.042	0.94

0.13	0.034	0.95
0.04	0.015	0.96

Besides, live observation of translocation experiment of rolling cycle amplification (RCA) products through 10×10 22 nm TPPs before and after lipid bilayer coating was implemented. The results can be found both in Figure 5.6. In the absence of lipid bilayer, the TPP array became clogged very quickly after adding RCA products and applying a 500 mV bias, due to the non-specific adsorption of RCA products on the TPP sidewall. In contrast, it is possible to detect the RCA translocation through each individual TPP for a few minutes without any pore clogging. This confirms that lipid bilayer can introduce non-fouling properties to the TPPs, which is crucial for real sensing applications.

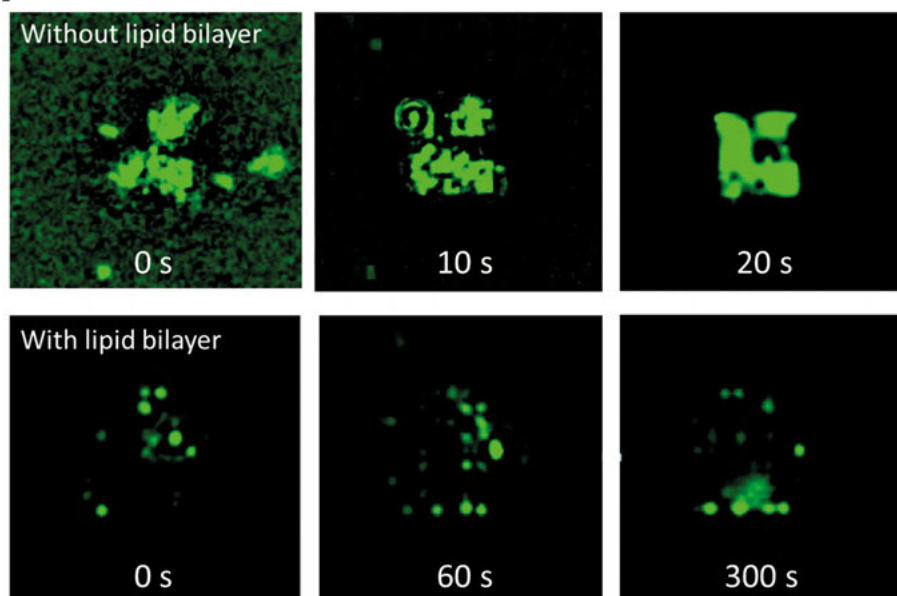


Figure 5.6. Live observation of rolling cycle amplification (RCA) products translocation experiment through 10×10 22 nm TPPs before and after lipid bilayer coating at 500 mV. Without lipid bilayer coating, the TPP array became clogged very quickly after adding RCA products and applying 500 mV bias. With the lipid bilayer coating, the TPPs are not clogged for a few minutes.

5.2 Multiple free-standing membranes with single nanopore on each

Although useful information can be extracted from the translocation events of numerous nanoparticles through multiple nanopores in a free-standing membrane simultaneously and randomly, individual addressability of each nanopore can further widen the applications of this technique. We have made an attempt of a novel design to integrate a solid-state nanopore array with microfluidics and a multiplexer, to enable individual addressability with fluidic and/or electrical control.

Nanopore arrays with 8×8 nanopores in free-standing SiN_x membranes were fabricated using our previous established fabrication process, as illustrated in Figure 5.7. Similar to the fabrication process presented in Chapter 3.2, arrayed nanopores were patterned by EBL and transferred to SiN_x by RIE. Arrayed $150\ \mu\text{m}$ windows on the backside were opened with alignment to the nanopores on the front side. After etching through the silicon substrate and stripping the oxide on the front side, arrays of free-standing membranes were formed with single nanopores on each of the free-standing membranes. The chips containing nanopore arrays were coated with a $10\ \text{nm}$ thick SiO_2 grown by means of ALD to avoid current leakage from pore to pore through the bulk silicon substrate during ionic current measurement. PDMS slab with casted fluid channels were aligned and bonded on both sides of the silicon chip in an orthogonal configuration.

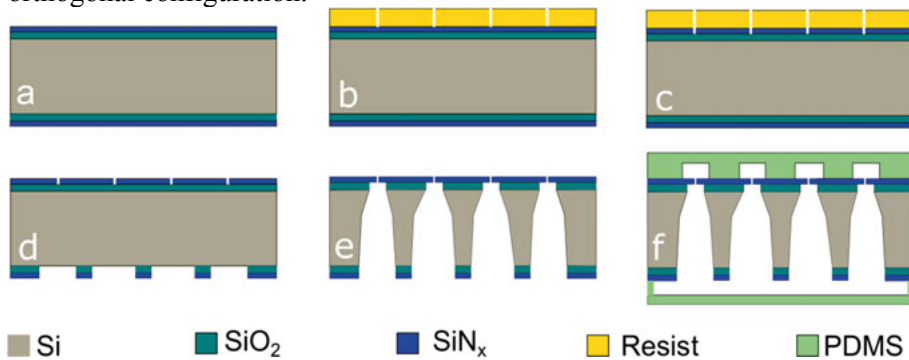


Figure 5.7. Schematic illustration of the fabrication process for nanopore array and PDMS bonding.

Figure 5.8(a) shows the optical images of both sides of the PDMS bonded chips. The rows and columns are orthogonally arranged to facilitate the individual addressability. Within each fluid channel, 8 free-standing membranes are located with only one nanopore on each membrane, as seen in Figure 5.8(b, ii-iii). The design of fluid connections with the bonded chip is shown in Figure 5.8(b). Ag/AgCl electrodes are embedded in each of the fluid outlet lines. Hence, measurement of any selected nanopore can be realized individually

either fluidically, by filling one channel on the top side (e.g. R1) and one channel on the bottom side (e.g. C2), or electrically, by applying bias on one channel on the top (e.g. R1) and grounding one channel on the bottom (e.g. C2) if all the fluid channels are filled with electrolytes. However, severe cross talk may arise when all the fluid channels are filled with electrolytes. Because all the nanopores are virtually connected through the fluid channels and an equivalent circuit comprising a 4×4 planar resistor network is illustrated Figure 5.9(a). For example, if R1 is selected by applying a bias, the current can also go through R2, R3 and R4. Overall, the total resistance between the two electrodes is $R_{total} = R_0 \left[\left(\frac{1}{3} + \frac{1}{9} + \frac{1}{3} \right) \parallel 1 \right] = \frac{7}{16} R_0$ assuming all the resistors have the same resistance R_0 . The total resistance is less than half of the resistance of R1. In order to resolve this issue, the potential of the unselected rows and columns should be controlled when sampling the voltage on the selected row and column, as shown in figure 5.9(b). For instance, when R1C1 is selected by applying a bias to C1 and grounding R1, the same bias should be applied to C2, C3 and C4 by a follower, and R2, R3 and R4 should be grounded,

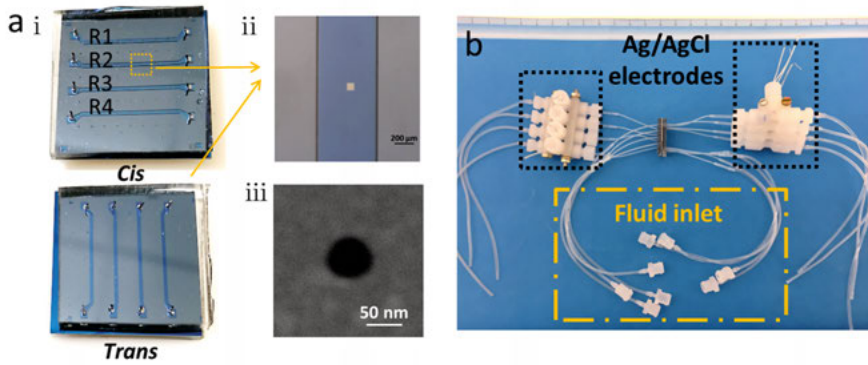


Figure 5.8. Optical images of a nanopore array chip bonded with PDMS (a) and fluid connections with embedded Ag/AgCl electrodes (b).

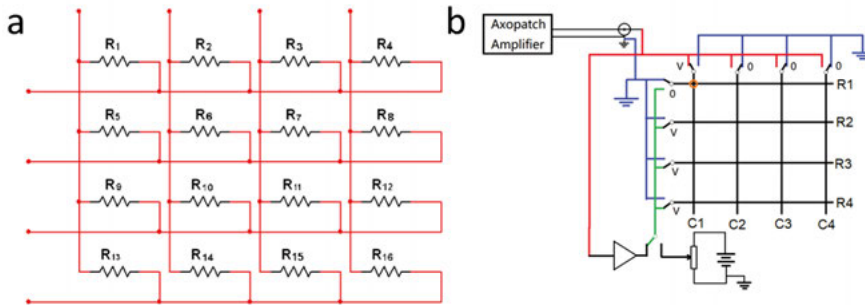


Figure 5.9. (a) Equivalent resistor network of a nanopore array with all the fluid channels filled with electrolyte, each resistor representing a nanopore. The resistance

contributed from the bulk electrolyte is neglected. (b) Potential control of the unselected columns and rows in the resistor network when applying a bias to the first row and first column.

Figure 5.10(a) shows the ionic current measurement results of four randomly chosen pores by fluidical selection. The four chosen pores display similar ionic current behaviors when switching on and off an applied 200 mV bias twice. Figure 5.10(b) shows the obtained conductance for 11 conductive nanopores from a 4×4 nanopore array with the same pore size by electrical selection. R1C2, R2C2, and R3C2 poorly conduct and R1C1 and R2C1 partially conduct, therefore not shown. The average conductance is calculated to be 14.4 ± 2.8 nS. According to Equation (2.3), the effective pore diameter is calculated as 85.3nm. The poor wettability of nanopore surface in electrolyte can cause air bubbles residing inside the nanopores and result in non-full conduction of the ionic solution [131], [132]. Pore wettability can be improved by a treatment of oxygen plasma and piranha solution cleaning. Besides, flushing mixture of ethanol and water several times can also help the pore wetting.

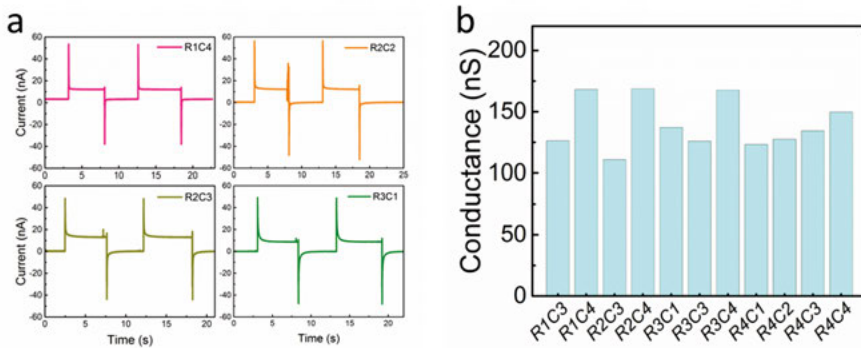


Figure 5.9. (a) Current trace of 4 different nanopores without and with applying a 200 mV bias by fluidical selection. The applied voltage is switched on and off twice for demonstration of reproducibility. (b) Conductance for 11 conductive nanopores of a 4×4 nanopore array by electrical selection.

Overall, a versatile platform to realize individually addressable solid-state nanopore array has been developed and demonstrated. Integration of microfluidics and custom-made multiplexer is key to this realization. Our fabrication and integration method can be easily scaled up by taking advantage of microelectronics and microfluidic technologies.

6. Summary and outlook

The work presented in this thesis concerns an exploration of various approaches to fabricating solid-state nanopores and subsequently exploring different applications of the fabricated nanopores. From the fabrication point of view, the main achievements in this thesis are:

- He FIB technique was employed to fabricate sub-10 nm nanopores in SiN_x membrane. He FIB was used instead of TEM due to its flexibility with different sample sizes. Although this fabrication technique cannot massively produce nanopores, it did provide us with the first sub-10 nm nanopore to enable our low-frequency noise studies of solid-state nanopores.
- A combination of EBL and RIE was used to achieve mass production of solid-state nanopores. These processes are compatible with the existing CMOS technology and the nanopores can be fabricated at the 4 inch wafer scale. The smallest diameter of nanopores reproducibly obtained with this technique is around 40 nm.
- Ion beam etching was also attempted to open up the possibilities of fabricating nanopores in other materials than those that are difficult to etch chemically.
- Anisotropic etching of silicon was successfully applied to controllably and reproducibly produce sub-10 nm nanopores in ultra-thin single-crystal silicon membranes. The anisotropic wet etching property of single crystal silicon helped to achieve much smaller actual pore size than the EBL defined size.
- EBICD was used to controllably reduce the size of pre-fabricated nanopores. Although deposited carbon is considered to be hydrophobic, a treatment of piranha cleaning and oxygen plasma can activate the surface, make it hydrophilic and allow for conducting current-voltage measurements in electrolytes.
- Lipid bilayer was studied to coat the TPPs in order to obtain a biologically relevant and well-defined surface of the nanopores. The anti-fouling property of the lipid bilayer was demonstrated to prevent non-specific adsorption of biomolecular analytes during translocation. Meanwhile, the size of the pores was also reduced by around 10 nm because of the thickness of the lipid bilayer and an interstitial water layer trapped between the bilayer and the support.

From the sensing application point of view, the main findings in this thesis are:

- Silica nanoparticles translocating a SiN_x nanopore with its size reduced by EBICD were demonstrated. The size reduced nanopores were found to be able to perform the translocation tests as smoothly as their sister SiN_x nanopores.
- DNA and protein translocation through TPPs were demonstrated. DNA translocation was found to be driven by electrophoretical force while protein translocation was driven by EOF. Numerical simulations revealed the formation of an electroosmotic vortex inside the TPPs and the vortex-protein interaction was found to play a decisive role in rectifying the translocation particularly in terms of translocation frequency
- TPPs were used to monitor enzymatic reaction by taking advantage of the truncated pyramidal shape of TPPs to localize an enzyme inside a TPP. Change of rectifying behavior of the ionic current through the TPP was observed as a result of surface charge density change caused by the local enzymatic reaction in the TPP.
- Multiple nanopores fabricated in a single free-standing membrane were used to study the group translocation behavior of nanoparticles and lipid bilayer formation. Although this method lacks individual addressability, useful information such as nanoparticle concentrations and kinetics of lipid bilayer formation can still be extracted from analysis of the ionic current traces.
- A novel design, enabling individual addressability with fluidic and/ or electrical control, was demonstrated by integrating a solid-state nanopore array with microfluidics and a multiplexer.

As discussed in the Introduction part, there are several challenges encountered in the nanopore field. The work presented in this thesis mainly concerns the fabrication aspect. More efforts can be made in the future to advance the wider applications of nanopore sensors, suggested as follows:

- Background noise of the ionic current measurements needs to be suppressed to pursue a high temporal resolution. Compared with biological nanopores, solid-state nanopores present a much higher background noise. A full understanding of the underlying mechanism of the noise is needed to control and reduce the noise generation.
- Functionalization of the nanopores can be performed to realize a high sensing selectivity of the analytes to be detected. For example, specific ligands can be tethered to the sidewall of the nanopore to enhance the interaction between the nanopore and analytes, thereby increasing selectivity and extending dwell time.
- 2D materials can be potentially combined to increase the spatial resolution of detection.

Sammanfattning på Svenska

Nanoporer är av stort intresse för studier av DNA-sekvensering, proteinprofilering, molekylseparation, jonselektiv filtrering, elkraftproduktion såväl som nano-mönstring. Nanoporer i fasta material har uppenbara fördelar jämfört med deras biologiska motsvarigheter när det gäller hög kemisk stabilitet och återanvändbarhet, kontrollerbarhet av geometri såväl som kompatibilitet med de befintliga teknikerna för halvledare och mikrofluidproduktion. Nanopordetektering är oftast baserad på att mäta jonström genom en nanopor medan man applicerar en spänning över den. När en analyt passerar genom poren förändras jonströmmen tillfälligt vilket ger information om analyten såsom dess storlek, form och ytladdning. Även om många storslagna rapporter om användning av nanoporer i fasta material har dykt upp i litteraturen, kvarstår fortfarande flera utmaningar för deras bredare tillämpningar. Dessa utmaningar inkluderar förbättring av reproducerbarheten vid tillverkning för massproduktion av ultra-små nanoporer och minimering av mätinstabiliteten samt kontroll av translokationshastighet och lägre bakgrundsljud.

Arbetet som presenteras i denna avhandling avser utforskande av olika tillvägagångssätt för att tillverka nanoporer i fasta material och därefter undersöka olika tillämpningar av de tillverkade nanoporerna. Ur tillverkningsynpunkt är de viktigaste resultaten i denna avhandling:

- He FIB-teknik användes för att tillverka sub-10 nm nanoporer i SiN_x -membran. He FIB användes istället för TEM på grund av dess flexibilitet med olika tillverkningsstorlekar. Även om denna tillverkningsteknik inte kan massproducera nanoporer, gav den oss den första sub-10 nm nanoporen för att möjliggöra våra studier av lågfrekvent brus hos nanoporer i fasta material.
- En kombination av EBL och RIE användes för att uppnå massproduktion av nanoporer i fasta material. Dessa processer är kompatibla med den existerande CMOS-tekniken och nanoporerna kan tillverkas på 4-tums skivor. Den minsta diametern på nanoporer som kan reproduceras med denna teknik är cirka 40 nm.
- Etsning av jonstrålar provades också för att öppna upp möjligheterna att tillverka nanoporer i andra material än de som är svåra att etsa kemiskt.
- Anisotropisk etsning av kisel användes framgångsrikt för att kontrollerbart och reproducerbart producera sub-10 nm nanoporer i ultratunna enkristallina kiselmembran. Den anisotropa egenskapen för våtetsning av

enkristallint kisel hjälpte att producera mycket mindre faktiska porstorlek än den EBL-definierade storleken.

- EBICD användes för att kontrollerbart minska storleken på förtillverkade nanoporer. Även om deponerat kol anses vara hydrofobt, kan en behandling av piranha-rengöring och syrgasplasma aktivera ytan, göra den hydrofil och möjliggöra ström-spänningsmätningar i elektrolyter.
- Dubbelskikt av lipider studerades för att belägga TPP:erna för att erhålla en biologiskt relevant och väldefinierad yta på nanoporerna. Anti-beläggningsegenskapen hos lipid-dubbelskiktet demonstrerades för att förhindra icke-specifik adsorption av biomolekylära analyter under translokation. Under tiden minskades porens storlek också med cirka 10 nm på grund av tjockleken hos lipid-dubbelskiktet och ett mellanliggande vattenskikt instängt mellan dubbelskiktet och bäraren.

Från detekterande applikationsaspekt är de viktigaste resultaten i denna avhandling:

- Kiseldioxidnanopartiklar som translokerar en SiN_x -nanopor med dess storlek reducerad med EBICD demonstrerades. De storleksminskade nanoporerna visade sig kunna utföra translokationstesterna lika smidigt som deras närbesläktade SiN_x -nanoporer.
- DNA och proteintranslokation genom TPP:er demonstrerades. DNA-translokation visade sig drivas av elektroforetisk kraft medan proteintranslokation drivs av EOF. Numeriska simuleringar avslöjar bildandet av en elektroosmotisk virvel inuti TPP:erna och virvel-proteininteraktionen har visat sig spela en avgörande roll för att korrigera translokationen, särskilt när det gäller translokationsfrekvens
- TPP:er användes för att övervaka enzymatisk reaktion genom att utnyttja den trunkerade pyramidformen hos TPP:er för att lokalisera ett enzym inuti ett TPP. Förändring av korrigerande beteende hos jonströmmen genom TPP observerades som ett resultat av förändring av ytladdningsdensitet orsakad av den lokala enzymatiska reaktionen i TPP.
- Flera nanoporer tillverkade i ett enda fristående membran användes för att studera grupptranslokationsbeteendet hos nanopartiklar och bildandet av lipid-dubbelskikt. Även om denna metod saknar individuell adresserbarhet, kan användbar information såsom nanopartikelkoncentrationer och kinetiken vid bildandet av lipid-dubbelskikt fortfarande extraheras från analys av jonströmmen.
- En ny design, som möjliggör individuell adresserbarhet med fluidisk och/eller elektrisk styrning, demonstrerades genom att integrera en uppsättning med nanoporer i fasta material med mikrofluidik och en multiplexer.

Som diskuterats tidigare finns det flera utmaningar inom området nanoporer. Det arbete som presenteras i denna avhandling avser främst tillverkningsaspekten. Fler ansträngningar kan göras i framtiden för att främja de bredare tillämpningarna av nanoporsensorer, där följande föreslås:

- Bakgrundsbrus från jonströmmätningarna måste undertryckas för att få en hög tidsupplösning. Jämfört med biologiska nanoporer ger nanoporer i fasta material ett mycket högre bakgrundsbrus. En fullständig förståelse av den underliggande mekanismen för brus behövs för att kontrollera och minska brusgenereringen.
- Funktionalisering av nanoporerna kan utföras för att uppnå en hög detektionssselektivitet hos de analyter som ska detekteras. Exempelvis kan specifika ligander knytas till nanoporens sidovägg för att förbättra interaktionen mellan nanoporen och analyterna, varigenom selektiviteten ökar och vistelsetiden förlängs.
- 2D-material kan potentiellt kombineras för att öka den rumsliga detektionsupplösningen.

Acknowledgement

First and foremost, I want to thank my main supervisor Prof. Zhen Zhang for your guidance, support and help throughout my PhD study. Thanks for providing me this opportunity of studying at Uppsala University. I also want to say many thanks to my co-supervisor Prof. Shili Zhang. I am inspired by your relentless passion and involvement towards research.

I want to sincerely thank all the people involved in the nanopore project. Chenyu Wen, thank you so much for all the discussions, support and help in the electrical measurements and simulations. Shiyu Li, thanks a lot for your patience and help in the preparation of my manuscript writing and optical measurements. Apart from being colleagues with you two in the lab, I treasured all the trips we travelled and all the fun time we had together. Paul Solomon, thank you very much for all the insightful discussions on my work. Prof. Klas Hjort, thanks for all the inspiration ideas you shared during the project meetings.

I want to say special thanks to Prof. Jörgen Olsson and Drags Dancila for screening my thesis and giving me useful comments for improvements. Thank Tomas Nyberg for translating the sammanfattning på svenska. I also appreciate all the efforts we have made together to the maintenance of the evaporator.

I want to particularly thank the staff at MSL and Electrum: Örjan Vallin, Amit Patel, Victoria Sternhagen, Rimantas Brucas, Leif Kuzavas, Farhad Zamany, Sven Noren, Björn Kuzavas, Ernesto Vargas Catalan, Yongbin Wang and Per-Erik Hellström. Thanks for all your help and support in the cleanroom. Without the introduction and the maintenances of the tools by you, this work would have not been possible. I also want to thank Johan Karl Andersson and Ulf Södervall for your assistance of silicon nitride deposition at Chalmers.

I want to thank Jonatan Bagge for the IT support, thank Lars Riekehr for the FIB preparation and TEM measurements, thank Ingrid Ringård and Ramy Salameh for all your administrative help.

I want to thank all my friends, former and current members in our group: Da Zhang, Xi Chen, Si Chen, Xingxing Xu, Qitao Hu, Yingtao Yu, Yifei Liu,

Yuan Zhu, Jiue Wu, Lukas Jablonka, Asta Makaraviciute, Nathan Netzer, Indrek Must, Chiao-Wei Teseng, Umut Cindemir and Quentin Palomar for your support, help and cooperation.

I want to thank my colleagues in our division: Uwe Zimmermann, Ngan Pham, Yao Yao, Wei-Chao Chen, Syaiful Redzewan Mohd Shah, Libo Chen, Ya Hu, Renbin Tong, Zhibin Zhang, Long Hoand Duc, Sven Englund, Malkolm Hin-nemo, Patrik Alberg, Michelle Marie Villamayor, Björn Landeke-Wilsmark, Carl Hägglund, Tomas Kubart, Tobias Törndahl, *etc* for all the taught courses and nice discussions around the lunch table.

I want to thank all my Chinese friends I have met in Sweden: Jie Zhao, Kai Song, Huan Wang, Ye Zou, Feiyan Liang, Qian Liu, Chengyu Wang, Yujing Wang, Jingyi Yu, Man Song, Rui Sun, Lei Tian, Youwei Zhang, Ruixue Zeng, Chi Zhang, Meiyuan Guo, Mingzhi Jiao, Zhenhua Liu, Shengyang Zhou, Xueying Kong, Lulu Wu, Peng Zhang, Chao Xu, Ruijun Pan, Haidong Liu, Pianpian Wu *etc* for all the nice time we had, all the trips we travelled, and playing badminton together. Special thanks to Lai Zeng and Liyun Yang for all your help, hosting and catering me so many times in Stockholm.

Finally, I want to thank Jiaqi Lu for all your care and support in my study and daily life. Thank my parents and brother for all your tolerance, support and love throughout my life.

Shuangshuang Zeng
曾双双

2019-12-16, Uppsala

References

- [1] “History of Medicine Timeline.” [Online]. Available: <http://www.datesandevents.org/events-timelines/10-history-of-medicine-timeline.htm>. [Accessed: 08-Oct-2019].
- [2] “The Human Genome Project,” *Genome.gov*. [Online]. Available: <https://www.genome.gov/human-genome-project>. [Accessed: 16-Oct-2019].
- [3] “DNA Sequencing Costs: Data,” *Genome.gov*. [Online]. Available: <https://www.genome.gov/about-genomics/fact-sheets/DNA-Sequencing-Costs-Data>. [Accessed: 17-Oct-2019].
- [4] R. Hodson, “Precision medicine,” *Nature*, vol. 537, pp. S49–S49, Sep. 2016.
- [5] M. U. Ahmed, I. Saaem, P. C. Wu, and A. S. Brown, “Personalized diagnostics and biosensors: a review of the biology and technology needed for personalized medicine,” *Critical Reviews in Biotechnology*, vol. 34, no. 2, pp. 180–196, Jun. 2014.
- [6] P. Mehrotra, “Biosensors and their applications – A review,” *Journal of Oral Biology and Craniofacial Research*, vol. 6, no. 2, pp. 153–159, May 2016.
- [7] V. Gaudin, “Advances in biosensor development for the screening of antibiotic residues in food products of animal origin – A comprehensive review,” *Biosensors and Bioelectronics*, vol. 90, pp. 363–377, Apr. 2017.
- [8] J. Tavakoli and Y. Tang, “Hydrogel Based Sensors for Biomedical Applications: An Updated Review,” in *Polymers*, 2017.
- [9] E. T. Powner and F. Yalcinkaya, “Intelligent biosensors,” *Sensor Review*, vol. 17, no. 2, pp. 107–116, Jan. 1997.
- [10] M. Muthukumar, C. Plesa, and C. Dekker, “Single-molecule sensing with nanopores,” *Physics Today*, vol. 68, no. 8, pp. 40–46, Jul. 2015.
- [11] F. Haque, J. Li, H.-C. Wu, X.-J. Liang, and P. Guo, “Solid-state and biological nanopore for real-time sensing of single chemical and sequencing of DNA,” *Nano Today*, vol. 8, no. 1, pp. 56–74, Feb. 2013.
- [12] D. W. Deamer and M. Akeson, “Nanopores and nucleic acids: prospects for ultrarapid sequencing,” *Trends in Biotechnology*, vol. 18, no. 4, pp. 147–151, Apr. 2000.
- [13] J. J. Kasianowicz, E. Brandin, D. Branton, and D. W. Deamer, “Characterization of individual polynucleotide molecules using a membrane channel,” *PNAS*, vol. 93, no. 24, pp. 13770–13773, Nov. 1996.
- [14] J. S. Retel *et al.*, “Structure of outer membrane protein G in lipid bilayers,” *Nature Communications*, vol. 8, no. 1, pp. 1–10, Dec. 2017.
- [15] M. Faller, M. Niederweis, and G. E. Schulz, “The Structure of a Mycobacterial Outer-Membrane Channel,” *Science*, vol. 303, no. 5661, pp. 1189–1192, Feb. 2004.

- [16] C. Cao, Y.-L. Ying, Z.-L. Hu, D.-F. Liao, H. Tian, and Y.-T. Long, "Discrimination of oligonucleotides of different lengths with a wild-type aerolysin nanopore," *Nature Nanotechnology*, vol. 11, no. 8, pp. 713–718, Aug. 2016.
- [17] M. Mueller, U. Grauschopf, T. Maier, R. Glockshuber, and N. Ban, "The structure of a cytolytic α -helical toxin pore reveals its assembly mechanism," *Nature*, vol. 459, no. 7247, pp. 726–730, Jun. 2009.
- [18] W. Shi, A. K. Friedman, and L. A. Baker, "Nanopore Sensing," *Anal. Chem.*, vol. 89, no. 1, pp. 157–188, Jan. 2017.
- [19] I. M. Derrington *et al.*, "Nanopore DNA sequencing with MspA," *PNAS*, vol. 107, no. 37, pp. 16060–16065, Sep. 2010.
- [20] "Oxford Nanopore Technologies." [Online]. Available: <https://nanoporetech.com/>. [Accessed: 13-Dec-2019].
- [21] L. Movileanu, S. Howorka, O. Braha, and H. Bayley, "Detecting protein analytes that modulate transmembrane movement of a polymer chain within a single protein pore," *Nature Biotechnology*, vol. 18, no. 10, pp. 1091–1095, Oct. 2000.
- [22] S. Cheley, H. Xie, and H. Bayley, "A Genetically Encoded Pore for the Stochastic Detection of a Protein Kinase," *ChemBioChem*, vol. 7, no. 12, pp. 1923–1927, 2006.
- [23] J. Etteedgui, J. J. Kasianowicz, and A. Balijepalli, "Single Molecule Discrimination of Heteropolytungstates and Their Isomers in Solution with a Nanometer-Scale Pore," *J. Am. Chem. Soc.*, vol. 138, no. 23, pp. 7228–7231, Jun. 2016.
- [24] L.-Q. Gu, O. Braha, S. Conlan, S. Cheley, and H. Bayley, "Stochastic sensing of organic analytes by a pore-forming protein containing a molecular adapter," *Nature*, vol. 398, no. 6729, pp. 686–690, Apr. 1999.
- [25] S. Wen *et al.*, "Highly Sensitive and Selective DNA-Based Detection of Mercury(II) with α -Hemolysin Nanopore," *J. Am. Chem. Soc.*, vol. 133, no. 45, pp. 18312–18317, Nov. 2011.
- [26] J. Li, D. Stein, C. McMullan, D. Branton, M. J. Aziz, and J. A. Golovchenko, "Ion-beam sculpting at nanometre length scales," *Nature*, vol. 412, no. 6843, p. 35084037, Jul. 2001.
- [27] M. J. Kim, M. Wanunu, D. C. Bell, and A. Meller, "Rapid Fabrication of Uniformly Sized Nanopores and Nanopore Arrays for Parallel DNA Analysis," *Adv. Mater.*, vol. 18, no. 23, pp. 3149–3153, Dec. 2006.
- [28] A. J. Storm, J. H. Chen, X. S. Ling, H. W. Zandbergen, and C. Dekker, "Fabrication of solid-state nanopores with single-nanometre precision," *Nature Materials*, vol. 2, no. 8, p. nmat941, Jul. 2003.
- [29] B. M. Venkatesan, A. B. Shah, J.-M. Zuo, and R. Bashir, "DNA Sensing Using Nanocrystalline Surface-Enhanced Al_2O_3 Nanopore Sensors," *Advanced Functional Materials*, vol. 20, no. 8, pp. 1266–1275, Apr. 2010.
- [30] C. A. Merchant *et al.*, "DNA Translocation through Graphene Nanopores," *Nano Letters*, vol. 10, no. 8, pp. 2915–2921, Aug. 2010.
- [31] K. Liu, J. Feng, A. Kis, and A. Radenovic, "Atomically Thin Molybdenum Disulfide Nanopores with High Sensitivity for DNA Translocation," *ACS Nano*, vol. 8, no. 3, pp. 2504–2511, Mar. 2014.
- [32] N. Varongchayakul, J. Song, A. Meller, and M. W. Grinstaff, "Single-molecule protein sensing in a nanopore: a tutorial," *Chem. Soc. Rev.*, vol. 47, no. 23, pp. 8512–8524, Nov. 2018.

- [33] E. C. Yusko *et al.*, “Real-time shape approximation and fingerprinting of single proteins using a nanopore,” *Nature Nanotechnology*, vol. 12, no. 4, pp. 360–367, Apr. 2017.
- [34] Y.-X. Hu, Y.-L. Ying, R. Gao, R.-J. Yu, and Y.-T. Long, “Characterization of the Dynamic Growth of the Nanobubble within the Confined Glass Nanopore,” *Anal. Chem.*, vol. 90, no. 21, pp. 12352–12355, Nov. 2018.
- [35] J. Feng *et al.*, “Identification of single nucleotides in MoS₂ nanopores,” *Nature Nanotechnology*, vol. 10, no. 12, pp. 1070–1076, Dec. 2015.
- [36] B. M. Venkatesan and R. Bashir, “Nanopore sensors for nucleic acid analysis,” *Nature Nanotechnology*, vol. 6, no. 10, pp. 615–624, Oct. 2011.
- [37] C. Plesa, S. W. Kowalczyk, R. Zinsmeister, A. Y. Grosberg, Y. Rabin, and C. Dekker, “Fast Translocation of Proteins through Solid State Nanopores,” *Nano Lett.*, vol. 13, no. 2, pp. 658–663, Feb. 2013.
- [38] J. K. Rosenstein, M. Wanunu, C. A. Merchant, M. Drndic, and K. L. Shepard, “Integrated nanopore sensing platform with sub-microsecond temporal resolution,” *Nat Methods*, vol. 9, no. 5, pp. 487–492, May 2012.
- [39] G. M. Cherf, K. R. Lieberman, H. Rashid, C. E. Lam, K. Karplus, and M. Akeson, “Automated forward and reverse ratcheting of DNA in a nanopore at 5-Å precision,” *Nat Biotechnol.*, vol. 30, no. 4, pp. 344–348, Apr. 2012.
- [40] E. A. Manrao *et al.*, “Reading DNA at single-nucleotide resolution with a mutant MspA nanopore and phi29 DNA polymerase,” *Nat Biotechnol.*, vol. 30, no. 4, pp. 349–353, Apr. 2012.
- [41] V. Tabard-Cossa, D. Trivedi, M. Wiggin, N. N. Jetha, and A. Marziali, “Noise analysis and reduction in solid-state nanopores,” *Nanotechnology*, vol. 18, no. 30, p. 305505, Jun. 2007.
- [42] V. Dimitrov *et al.*, “Nanopores in solid-state membranes engineered for single molecule detection,” *Nanotechnology*, vol. 21, no. 6, p. 065502, Jan. 2010.
- [43] K. Venta *et al.*, “Differentiation of Short, Single-Stranded DNA Homopolymers in Solid-State Nanopores,” *ACS Nano*, vol. 7, no. 5, pp. 4629–4636, May 2013.
- [44] W. H. Pitchford *et al.*, “Synchronized Optical and Electronic Detection of Biomolecules Using a Low Noise Nanopore Platform,” *ACS Nano*, vol. 9, no. 2, pp. 1740–1748, Feb. 2015.
- [45] T. Jain, R. J. S. Guerrero, C. A. Aguilar, and R. Karnik, “Integration of Solid-State Nanopores in Microfluidic Networks via Transfer Printing of Suspended Membranes,” *Anal. Chem.*, vol. 85, no. 8, pp. 3871–3878, Apr. 2013.
- [46] S. Garaj, W. Hubbard, A. Reina, J. Kong, D. Branton, and J. A. Golovchenko, “Graphene as a subnanometre trans-electrode membrane,” *Nature*, vol. 467, no. 7312, pp. 190–193, Sep. 2010.
- [47] K. Briggs *et al.*, “DNA Translocations through Nanopores under Nanoscale Preconfinement,” *Nano Lett.*, vol. 18, no. 2, pp. 660–668, Feb. 2018.
- [48] E. C. Yusko *et al.*, “Controlling protein translocation through nanopores with bio-inspired fluid walls,” *Nature Nanotechnology*, vol. 6, no. 4, p. nnano.2011.12, Feb. 2011.
- [49] M. Charron, K. Briggs, S. King, M. Waugh, and V. Tabard-Cossa, “Precise DNA Concentration Measurements with Nanopores by Controlled Counting,” *Anal. Chem.*, vol. 91, no. 19, pp. 12228–12237, Oct. 2019.
- [50] W. H. Coulter, “Means for counting particles suspended in a fluid,” 2656508, 20-Oct-1953.

- [51] V. Tabard-Cossa, "Chapter 3 - Instrumentation for Low-Noise High-Bandwidth Nanopore Recording," in *Engineered Nanopores for Bioanalytical Applications*, J. B. Edel and T. Albrecht, Eds. Oxford: William Andrew Publishing, 2013, pp. 59–93.
- [52] J. D. Uram, K. Ke, and M. Mayer, "Noise and Bandwidth of Current Recordings from Submicrometer Pores and Nanopores," *ACS Nano*, vol. 2, no. 5, pp. 857–872, May 2008.
- [53] F. N. Hooge, "1/f noise," *Physica B+C*, vol. 83, no. 1, pp. 14–23, May 1976.
- [54] F. N. Hooge, "1/f noise is no surface effect," *Physics Letters A*, vol. 29, no. 3, pp. 139–140, Apr. 1969.
- [55] A. T. Carlsen, O. K. Zahid, J. Ruzicka, E. W. Taylor, and A. R. Hall, "Interpreting the Conductance Blockades of DNA Translocations through Solid-State Nanopores," *ACS Nano*, vol. 8, no. 5, pp. 4754–4760, May 2014.
- [56] S. W. Kowalczyk, A. Y. Grosberg, Y. Rabin, and C. Dekker, "Modeling the conductance and DNA blockade of solid-state nanopores," *Nanotechnology*, vol. 22, no. 31, p. 315101, Jul. 2011.
- [57] J. E. Hall, "Access resistance of a small circular pore.," *The Journal of General Physiology*, vol. 66, no. 4, pp. 531–532, Oct. 1975.
- [58] C. Wen, Z. Zhang, and S.-L. Zhang, "Physical Model for Rapid and Accurate Determination of Nanopore Size via Conductance Measurement," *ACS Sens.*, vol. 2, no. 10, pp. 1523–1530, Oct. 2017.
- [59] E. M. Ney, C.-H. Hou, and P. Taboada-Serrano, "Calculation of Electrical Double Layer Potential Profiles in Nanopores from Grand Canonical Monte Carlo Simulations," *J. Chem. Eng. Data*, vol. 63, no. 7, pp. 2557–2566, Jul. 2018.
- [60] R. J. Hunter, *Foundations of Colloid Science*, Second Edition. Oxford, New York: Oxford University Press, 2000.
- [61] R. B. Schoch, J. Han, and P. Renaud, "Transport phenomena in nanofluidics," *Rev. Mod. Phys.*, vol. 80, no. 3, pp. 839–883, Jul. 2008.
- [62] R. J. Hunter, *Zeta potential in colloid science : principles and applications* /. London : Academic Press, 1981.
- [63] D. P. Hoogerheide, S. Garaj, and J. A. Golovchenko, "Probing Surface Charge Fluctuations with Solid-State Nanopores," *Physical Review Letters*, vol. 102, no. 25, Jun. 2009.
- [64] J.-P. Cloarec *et al.*, "pH driven addressing of silicon nanowires onto Si₃N₄/SiO₂micro-patterned surfaces," *Nanotechnology*, vol. 27, no. 29, p. 295602, Jun. 2016.
- [65] R. W. O'Brien and L. R. White, "Electrophoretic mobility of a spherical colloidal particle," *J. Chem. Soc., Faraday Trans. 2*, vol. 74, no. 0, pp. 1607–1626, Jan. 1978.
- [66] M. H. Oddy and J. G. Santiago, "A method for determining electrophoretic and electroosmotic mobilities using AC and DC electric field particle displacements," *Journal of Colloid and Interface Science*, vol. 269, no. 1, pp. 192–204, Jan. 2004.
- [67] A. J. O'Connor, H. R. C. Pratt, and G. W. Stevens, "Electrophoretic mobilities of proteins and protein mixtures in porous membranes," *Chemical Engineering Science*, vol. 51, no. 13, pp. 3459–3477, Jul. 1996.

- [68] P. D. Ross and R. L. Scruggs, "Electrophoresis of DNA. III. The effect of several univalent electrolytes on the mobility of DNA," *Biopolymers*, vol. 2, no. 3, pp. 231–236, 1964.
- [69] S. B. Smith and A. J. Bendich, "Electrophoretic charge density and persistence length of DNA as measured by fluorescence microscopy," *Biopolymers*, vol. 29, no. 8–9, pp. 1167–1173, 1990.
- [70] M. Firnkes, D. Pedone, J. Knezevic, M. Döblinger, and U. Rant, "Electrically Facilitated Translocations of Proteins through Silicon Nitride Nanopores: Conjoint and Competitive Action of Diffusion, Electrophoresis, and Electroosmosis," *Nano Letters*, vol. 10, no. 6, pp. 2162–2167, Jun. 2010.
- [71] P. Waduge *et al.*, "Nanopore-Based Measurements of Protein Size, Fluctuations, and Conformational Changes," *ACS Nano*, vol. 11, no. 6, pp. 5706–5716, Jun. 2017.
- [72] S. Zeng, C. Wen, P. Solomon, S.-L. Zhang, and Z. Zhang, "Rectification of protein translocation in truncated pyramidal nanopores," *Nat. Nanotechnol.*, pp. 1–7, Oct. 2019.
- [73] J. Gierak *et al.*, "Sub-5nm FIB direct patterning of nanodevices," *Microelectronic Engineering*, vol. 84, no. 5, pp. 779–783, May 2007.
- [74] M. M. Marshall, J. Yang, and A. R. Hall, "Direct and Transmission Milling of Suspended Silicon Nitride Membranes With a Focused Helium Ion Beam," *Scanning*, vol. 34, no. 2, pp. 101–106, 2012.
- [75] H. Kwok, K. Briggs, and V. Tabard-Cossa, "Nanopore Fabrication by Controlled Dielectric Breakdown," *PLOS ONE*, vol. 9, no. 3, p. e92880, Mar. 2014.
- [76] A. Zrehen, T. Gilboa, and A. Meller, "Real-time visualization and sub-diffraction limit localization of nanometer-scale pore formation by dielectric breakdown," *Nanoscale*, vol. 9, no. 42, pp. 16437–16445, Nov. 2017.
- [77] J. Chen, T. Deng, C. N. Wu, and Z. W. Liu, "Fabrication of Silicon Nanopore Arrays with Three-Step Wet Etching," *ECS Trans.*, vol. 52, no. 1, pp. 371–376, Mar. 2013.
- [78] Z. Siwy, D. Dobrev, R. Neumann, C. Trautmann, and K. Voss, "Electro-responsive asymmetric nanopores in polyimide with stable ion-current signal," *Appl Phys A*, vol. 76, no. 5, pp. 781–785, Mar. 2003.
- [79] D. V. Verschuere, W. Yang, and C. Dekker, "Lithography-based fabrication of nanopore arrays in freestanding SiN and graphene membranes," *Nanotechnology*, vol. 29, no. 14, p. 145302, 2018.
- [80] P. Chen, T. Mitsui, D. B. Farmer, J. Golovchenko, R. G. Gordon, and D. Branton, "Atomic Layer Deposition to Fine-Tune the Surface Properties and Diameters of Fabricated Nanopores," *Nano Lett.*, vol. 4, no. 7, pp. 1333–1337, Jul. 2004.
- [81] R. Wei, D. Pedone, A. Zürner, M. Döblinger, and U. Rant, "Fabrication of Metallized Nanopores in Silicon Nitride Membranes for Single-Molecule Sensing," *Small*, vol. 6, no. 13, pp. 1406–1414, Jul. 2010.
- [82] M. Zhang, T. Schmidt, F. Sangghaleh, N. Roxhed, I. Sychugov, and J. Linnros, "Oxidation of nanopores in a silicon membrane: self-limiting formation of sub-10 nm circular openings," *Nanotechnology*, vol. 25, no. 35, p. 355302, Aug. 2014.
- [83] D. Stein, J. Li, and J. A. Golovchenko, "Ion-Beam Sculpting Time Scales," *Phys. Rev. Lett.*, vol. 89, no. 27, p. 276106, Dec. 2002.

- [84] M. J. Kim, B. McNally, K. Murata, and A. Meller, "Characteristics of solid-state nanometre pores fabricated using a transmission electron microscope," *Nanotechnology*, vol. 18, no. 20, p. 205302, Apr. 2007.
- [85] J. Shim, J. A. Rivera, and R. Bashir, "Electron beam induced local crystallization of HfO₂ nanopores for biosensing applications," *Nanoscale*, vol. 5, no. 22, pp. 10887–10893, Oct. 2013.
- [86] M. D. Fischbein and M. Drndić, "Sub-10 nm Device Fabrication in a Transmission Electron Microscope," *Nano Lett.*, vol. 7, no. 5, pp. 1329–1337, May 2007.
- [87] C. J. Lo, T. Aref, and A. Bezryadin, "Fabrication of symmetric sub-5 nm nanopores using focused ion and electron beams," *Nanotechnology*, vol. 17, no. 13, pp. 3264–3267, Jun. 2006.
- [88] A. Hemamouche *et al.*, "FIB patterning of dielectric, metallized and graphene membranes: A comparative study," *Microelectronic Engineering*, vol. 121, pp. 87–91, Jun. 2014.
- [89] J. Feng *et al.*, "Electrochemical Reaction in Single Layer MoS₂: Nanopores Opened Atom by Atom," *Nano Lett.*, vol. 15, no. 5, pp. 3431–3438, May 2015.
- [90] Q. Chen, Y. Wang, T. Deng, and Z. Liu, "Fabrication of nanopores and nanoslits with feature sizes down to 5 nm by wet etching method," *Nanotechnology*, vol. 29, no. 8, p. 085301, 2018.
- [91] Z. Siwy and A. Fuliński, "Fabrication of a Synthetic Nanopore Ion Pump," *Phys. Rev. Lett.*, vol. 89, no. 19, p. 198103, Oct. 2002.
- [92] C. C. Harrell, Y. Choi, L. P. Horne, L. A. Baker, Z. S. Siwy, and C. R. Martin, "Resistive-Pulse DNA Detection with a Conical Nanopore Sensor," *Langmuir*, vol. 22, no. 25, pp. 10837–10843, Dec. 2006.
- [93] P. Apel, "Track etching technique in membrane technology," *Radiation Measurements*, vol. 34, no. 1, pp. 559–566, Jun. 2001.
- [94] L. Petrossian, S. J. Wilk, P. Joshi, S. Hihath, S. M. Goodnick, and T. J. Thornton, "Fabrication of Cylindrical Nanopores and Nanopore Arrays in Silicon-On-Insulator Substrates," *Journal of Microelectromechanical Systems*, vol. 16, no. 6, pp. 1419–1428, Dec. 2007.
- [95] J. Bai *et al.*, "Fabrication of sub-20 nm nanopore arrays in membranes with embedded metal electrodes at wafer scales," *Nanoscale*, vol. 6, no. 15, pp. 8900–8906, 2014.
- [96] N. A. W. Bell and U. F. Keyser, "Specific Protein Detection Using Designed DNA Carriers and Nanopores," *J. Am. Chem. Soc.*, vol. 137, no. 5, pp. 2035–2041, Feb. 2015.
- [97] R. D. Bulushev, S. Marion, and A. Radenovic, "Relevance of the Drag Force during Controlled Translocation of a DNA–Protein Complex through a Glass Nanocapillary," *Nano Lett.*, vol. 15, no. 10, pp. 7118–7125, Oct. 2015.
- [98] Y.-L. Ying *et al.*, "Manipulating and visualizing the dynamic aggregation-induced emission within a confined quartz nanopore," *Nat Commun*, vol. 9, no. 1, pp. 1–6, Sep. 2018.
- [99] J. Yang *et al.*, "Rapid and precise scanning helium ion microscope milling of solid-state nanopores for biomolecule detection," *Nanotechnology*, vol. 22, no. 28, p. 285310, Jun. 2011.

- [100] H. Seidel, L. Csepregi, A. Heuberger, and H. Baumgärtel, "Anisotropic Etching of Crystalline Silicon in Alkaline Solutions I. Orientation Dependence and Behavior of Passivation Layers," *J. Electrochem. Soc.*, vol. 137, no. 11, pp. 3612–3626, Nov. 1990.
- [101] K. E. Petersen, "Silicon as a mechanical material," *Proceedings of the IEEE*, vol. 70, no. 5, pp. 420–457, May 1982.
- [102] P. Pal and K. Sato, "A comprehensive review on convex and concave corners in silicon bulk micromachining based on anisotropic wet chemical etching," *Micro and Nano Systems Letters*, vol. 3, no. 1, p. 6, May 2015.
- [103] W. M. Haynes, *CRC Handbook of Chemistry and Physics*. CRC Press, 2011.
- [104] D. B. Lee, "Anisotropic Etching of Silicon," *Journal of Applied Physics*, vol. 40, no. 11, pp. 4569–4574, Oct. 1969.
- [105] A. Kumao, H. Hashimoto, and K. Shiraishi, "Studies on Specimen Contamination by Transmission Electron Microscopy," *J Electron Microscop (Tokyo)*, vol. 30, no. 3, pp. 161–170, Jan. 1981.
- [106] A. E. Ennos, "The origin of specimen contamination in the electron microscope," *Br. J. Appl. Phys.*, vol. 4, no. 4, pp. 101–106, Apr. 1953.
- [107] A. N. Broers, W. W. Molzen, J. J. Cuomo, and N. D. Wittels, "Electron-beam fabrication of 80-Å metal structures," *Appl. Phys. Lett.*, vol. 29, no. 9, pp. 596–598, Nov. 1976.
- [108] F. Banhart, "The Formation of a Connection between Carbon Nanotubes in an Electron Beam," *Nano Lett.*, vol. 1, no. 6, pp. 329–332, Jun. 2001.
- [109] M. S. Wang, L.-M. Peng, J. Y. Wang, and Q. Chen, "Shaping Carbon Nanotubes and the Effects on Their Electrical and Mechanical Properties," *Advanced Functional Materials*, vol. 16, no. 11, pp. 1462–1468, 2006.
- [110] R. Kox, C. Chen, G. Maes, L. Lagae, and G. Borghs, "Shrinking solid-state nanopores using electron-beam-induced deposition," *Nanotechnology*, vol. 20, no. 11, p. 115302, 2009.
- [111] A. S. Prabhu, K. J. Freedman, J. W. F. Robertson, Z. Nikolov, J. J. Kasianowicz, and M. J. Kim, "SEM-induced shrinking of solid-state nanopores for single molecule detection," *Nanotechnology*, vol. 22, no. 42, p. 425302, Sep. 2011.
- [112] W. M. Zhang *et al.*, "Controllable shrinking and shaping of silicon nitride nanopores under electron irradiation," *Appl. Phys. Lett.*, vol. 90, no. 16, p. 163102, Apr. 2007.
- [113] S. Zeng *et al.*, "Controlled size reduction and its underlying mechanism to form solid-state nanopores via electron beam induced carbon deposition," *Nanotechnology*, vol. 30, no. 45, p. 455303, Aug. 2019.
- [114] T. Bret, S. Mauron, I. Utke, and P. Hoffmann, "Characterization of focused electron beam induced carbon deposits from organic precursors," *Microelectronic Engineering*, vol. 78–79, pp. 300–306, Mar. 2005.
- [115] V. Scheuer, H. Koops, and T. Tschudi, "Electron beam decomposition of carbonyls on silicon," *Microelectronic Engineering*, vol. 5, no. 1, pp. 423–430, Dec. 1986.
- [116] D. A. Alman, D. N. Ruzic, and J. N. Brooks, "A hydrocarbon reaction model for low temperature hydrogen plasmas and an application to the Joint European Torus," *Physics of Plasmas*, vol. 7, no. 5, pp. 1421–1432, Apr. 2000.

- [117] H. Demers *et al.*, “Three-dimensional electron microscopy simulation with the CASINO Monte Carlo software,” *Scanning*, vol. 33, no. 3, pp. 135–146, 2011.
- [118] E. Reimhult, F. Höök, and B. Kasemo, “Intact Vesicle Adsorption and Supported Biomembrane Formation from Vesicles in Solution: Influence of Surface Chemistry, Vesicle Size, Temperature, and Osmotic Pressure,” *Langmuir*, vol. 19, no. 5, pp. 1681–1691, Mar. 2003.
- [119] B. A. Lewis and D. M. Engelman, “Lipid bilayer thickness varies linearly with acyl chain length in fluid phosphatidylcholine vesicles,” *Journal of Molecular Biology*, vol. 166, no. 2, pp. 211–217, May 1983.
- [120] N. Kučerka, M.-P. Nieh, and J. Katsaras, “Fluid phase lipid areas and bilayer thicknesses of commonly used phosphatidylcholines as a function of temperature,” *Biochimica et Biophysica Acta (BBA) - Biomembranes*, vol. 1808, no. 11, pp. 2761–2771, Nov. 2011.
- [121] O. M. Eggenberger *et al.*, “Fluid surface coatings for solid-state nanopores: comparison of phospholipid bilayers and archaea-inspired lipid monolayers,” *Nanotechnology*, vol. 30, no. 32, p. 325504, May 2019.
- [122] J. Kong *et al.*, “Silicon Nitride Nanopores for Nanoparticle Sensing,” *Journal of Nanoscience and Nanotechnology*, vol. 13, no. 6, pp. 4010–4016, Jun. 2013.
- [123] G. Goyal, K. J. Freedman, and M. J. Kim, “Gold Nanoparticle Translocation Dynamics and Electrical Detection of Single Particle Diffusion Using Solid-State Nanopores,” *Anal. Chem.*, vol. 85, no. 17, pp. 8180–8187, Sep. 2013.
- [124] M. Davenport *et al.*, “The Role of Pore Geometry in Single Nanoparticle Detection,” *ACS Nano*, vol. 6, no. 9, pp. 8366–8380, Sep. 2012.
- [125] H. Oana, K. Tsumoto, Y. Yoshikawa, and K. Yoshikawa, “Folding transition of large DNA completely inhibits the action of a restriction endonuclease as revealed by single-chain observation,” *FEBS Letters*, vol. 530, no. 1, pp. 143–146, Oct. 2002.
- [126] Y. Qiu, Z. S. Siwy, and M. Wanunu, “Abnormal Ionic-Current Rectification Caused by Reversed Electroosmotic Flow under Viscosity Gradients across Thin Nanopores,” *Anal. Chem.*, vol. 91, no. 1, pp. 996–1004, Jan. 2019.
- [127] S. B. Bankar, M. V. Bule, R. S. Singhal, and L. Ananthanarayan, “Glucose oxidase — An overview,” *Biotechnology Advances*, vol. 27, no. 4, pp. 489–501, Jul. 2009.
- [128] D. Chen *et al.*, “Fabrication of Activity-Reporting Glucose Oxidase Nanocapsules with Oxygen-Independent Fluorescence Variation,” *ACS Appl. Mater. Interfaces*, vol. 10, no. 31, pp. 26005–26015, Aug. 2018.
- [129] E. Simoen, B. Kaczer, M. Toledano-Luque, and C. Claeys, “(Invited) Random Telegraph Noise: From a Device Physicist’s Dream to a Designer’s Nightmare,” *ECS Trans.*, vol. 39, no. 1, pp. 3–15, Sep. 2011.
- [130] C. Wen, S. Zeng, Z. Zhang, and S.-L. Zhang, “Group behavior of nanoparticles translocating multiple nanopores,” *Anal. Chem.*, Oct. 2018.
- [131] N. A. W. Bell *et al.*, “Multiplexed ionic current sensing with glass nanopores,” *Lab on a Chip*, vol. 13, no. 10, pp. 1859–1862, 2013.
- [132] E. Beamish, H. Kwok, V. Tabard-Cossa, and M. Godin, “Fine-tuning the Size and Minimizing the Noise of Solid-state Nanopores,” *JoVE (Journal of Visualized Experiments)*, no. 80, pp. e51081–e51081, Oct. 2013.

Acta Universitatis Upsaliensis

*Digital Comprehensive Summaries of Uppsala Dissertations
from the Faculty of Science and Technology 1890*

Editor: The Dean of the Faculty of Science and Technology

A doctoral dissertation from the Faculty of Science and Technology, Uppsala University, is usually a summary of a number of papers. A few copies of the complete dissertation are kept at major Swedish research libraries, while the summary alone is distributed internationally through the series Digital Comprehensive Summaries of Uppsala Dissertations from the Faculty of Science and Technology. (Prior to January, 2005, the series was published under the title "Comprehensive Summaries of Uppsala Dissertations from the Faculty of Science and Technology".)



ACTA
UNIVERSITATIS
UPSALIENSIS
UPPSALA
2020

Distribution: publications.uu.se
urn:nbn:se:uu:diva-399726